

This item is the archived peer-reviewed author-version of:

Deactivation study of $Fe_2O_3 - CeO_2$ during redox cycles for CO production from CO_2

Reference:

Dharanipragada N. V. R. Aditya, Meledina Maria, Galvita Vladimir V., Poelman Hilde, Turner Stuart, Van Tendeloo Gustaaf, Detavernier Christophe, Marin Guy B.- Deactivation study of $Fe_2O_3 - CeO_2$ during redox cycles for CO production from CO_2

Industrial and engineering chemistry research - ISSN 0888-5885 - 55:20(2016), p. 5911-5922

Full text (Publishers DOI): <http://dx.doi.org/doi:10.1021/acs.iecr.6b00963>

To cite this reference: <http://hdl.handle.net/10067/1342140151162165141>

Deactivation study of Fe₂O₃-CeO₂ during redox cycles for CO production from CO₂

Naga Venkata Ranga Aditya Dharanipragada, Maria Meledina, Vladimir V. Galvita, Hilde Poelman, Stuart Turner, Gustaaf Van Tendeloo, Christophe Detavernier, and Guy B Marin

Ind. Eng. Chem. Res., **Just Accepted Manuscript** • DOI: 10.1021/acs.iecr.6b00963 • Publication Date (Web): 22 Apr 2016

Downloaded from <http://pubs.acs.org> on April 27, 2016

Just Accepted

“Just Accepted” manuscripts have been peer-reviewed and accepted for publication. They are posted online prior to technical editing, formatting for publication and author proofing. The American Chemical Society provides “Just Accepted” as a free service to the research community to expedite the dissemination of scientific material as soon as possible after acceptance. “Just Accepted” manuscripts appear in full in PDF format accompanied by an HTML abstract. “Just Accepted” manuscripts have been fully peer reviewed, but should not be considered the official version of record. They are accessible to all readers and citable by the Digital Object Identifier (DOI®). “Just Accepted” is an optional service offered to authors. Therefore, the “Just Accepted” Web site may not include all articles that will be published in the journal. After a manuscript is technically edited and formatted, it will be removed from the “Just Accepted” Web site and published as an ASAP article. Note that technical editing may introduce minor changes to the manuscript text and/or graphics which could affect content, and all legal disclaimers and ethical guidelines that apply to the journal pertain. ACS cannot be held responsible for errors or consequences arising from the use of information contained in these “Just Accepted” manuscripts.

Deactivation study of Fe₂O₃-CeO₂ during redox cycles for CO production from CO₂

N.V.R. Aditya Dharanipragada^a, Maria Meledina^b, Vladimir V. Galvita^{a}, Hilde Poelman^a,
Stuart Turner^b, Gustaaf Van Tendeloo^b, Christophe Detavernier^c, and Guy B. Marin^a*

^aLaboratory for Chemical Technology, Ghent University, Technologiepark 914, B-9052 Gent, Belgium.

^bElectron Microscopy for Materials Science (EMAT), Department of Physics, University of Antwerp, Groenenborgerlaan 171, B-2020 Antwerp, Belgium.

^cDepartment of Solid State Sciences, Ghent University, Krijgslaan 281, S1, B-9000 Ghent, Belgium

*Corresponding author: E-mail address: Vladimir.Galvita@Ugent.be

Abstract

Deactivation was investigated in Fe₂O₃-CeO₂ oxygen storage materials during repeated H₂-reduction and CO₂-reoxidation. In situ XRD, XAS and TEM were used to identify phases, crystallite sizes and morphological changes upon cycling operation. The effect of redox cycling was investigated both in Fe-rich (80wt% Fe₂O₃-CeO₂) and Ce-rich (10wt%Fe₂O₃-CeO₂) materials. The former consisted of 100nm Fe₂O₃ particles decorated with 5-10nm Ce_{1-x}Fe_xO_{2-x}. The latter presented CeO₂ with incorporated Fe, i.e. a solid solution of Ce_{1-x}Fe_xO_{2-x}, as main

1
2
3 oxygen carrier. By modelling the EXAFS Ce-K signal for as prepared 10wt%Fe₂O₃-CeO₂, the
4 amount of Fe in CeO₂ was determined as 21mol%, corresponding to 86% of the total iron
5 content. Sintering and solid-solid transformations, the latter including both new phase formation
6 and element segregation, were identified as deactivation pathways upon redox cycling. In Ce-
7 rich material, perovskite (CeFeO₃) was identified by XRD. This phase remained inert during
8 reduction and reoxidation, resulting in an overall lower oxygen storage capacity. Further, Fe
9 segregated from the solid solution, thereby decreasing its reducibility. In addition, an increase in
10 crystallite size occurred for all phases. In Fe-rich material, sintering is the main deactivation
11 pathway, although Fe segregation from the solid solution and perovskite formation cannot be
12 excluded.
13
14
15
16
17
18
19
20
21
22
23
24
25
26
27
28
29
30

31 **Keywords:** Deactivation, Sintering, solid-solid transformation, in situ XRD, XAS.
32
33
34
35
36

37 **1.0 Introduction**

38
39 With rising global temperatures, the necessity to reduce greenhouse gas emissions like CO₂ has
40 only gained significance. Several technologies have been proposed to minimize CO₂ emissions¹⁻
41
42
43
44
45 ³. One such technology, which can utilize directly CO₂ by converting it to value added fuels is
46 chemical looping⁴⁻⁶, a cyclic redox process based on the regeneration of oxygen storage
47 materials. In the first half-cycle, gases such as CH₄ are employed to reduce the oxygen storage
48 material, resulting in the production of CO₂ and H₂O. The latter are used in the second half-cycle
49 for the regeneration of the oxygen storage material. When CO₂ is used as reoxidation agent this
50 results in the production of CO, which is a useful raw material, e.g. for Fischer-Tropsch
51
52
53
54
55
56
57
58
59
60

1
2
3 processes. Since the amount of CO₂ utilized in the second step is much higher than produced in
4
5 the first step, the process is termed CO₂ utilization^{7,8}.
6
7

8
9 The process economics of chemical looping are limited by the stability of the oxygen storage
10 materials. There are many paths towards the deactivation of oxygen storage materials. For
11 example, a material may be poisoned by a contaminant present in the reducing or oxidizing
12 agents. Its surface, pores and voids may be fouled by carbon produced during
13 cracking/condensation if hydrocarbon or carbon monoxide reactants are used for reduction. Due
14 to the high temperature of operation in chemical looping (T > 650°C), thermal degradation may
15 occur in the form of active phase crystallite growth, i.e. sintering, collapse of the pore structure
16 and/or solid-state reactions of the active phase with the carrier or modifying element. Hence, the
17 choice of oxygen storage material and modifying element towards chemical looping play a
18 crucial role.
19
20
21
22
23
24
25
26
27
28
29
30
31

32 Oxides of transition metals, such as Ni, Cu, Mo and Fe, are typically used as oxygen carriers.
33 Among these, iron oxides stand out because of their natural abundance and high reoxidation
34 capacity with CO₂ over a wide range of operating conditions (700°C -1000°C)⁹⁻¹¹. However, pure
35 iron oxides tend to deactivate rapidly. The major factor for deactivation in pure iron oxide
36 materials is sintering¹²⁻¹³.
37
38
39
40
41
42
43

44 To overcome this challenge, iron oxides are often modified with other oxide materials, e.g.
45 CeO₂^{14, 15}, CeZrO₂¹⁶, MgO¹⁷, Al₂O₃^{18, 19}, ZrO₂²⁰, SiO₂²¹, TiO₂²² and MgAl₂O₄²⁴⁻²⁶. These
46 promoter materials prevent contact between adjacent iron oxide particles, resulting in relatively
47 stable particle size, and are therefore termed as physical textural promoters. They mitigate
48 sintering by acting as a physical barrier. However, during a prolonged cyclic process, some
49 promoters can undergo solid-solid transformations with iron oxide, e.g. MgO to MgFe₂O₄, Al₂O₃
50
51
52
53
54
55
56
57
58
59
60

1
2
3 to FeAl_2O_4 and CeO_2 to perovskite (CeFeO_3). These new phases continue to prevent sintering by
4 providing a physical barrier between adjacent iron oxide particles, but reduce the total oxygen
5 storage capacity because the iron oxide involved in solid-solid transformations no longer
6 contributes. For Fe_2O_3 with Al_2O_3 , iron oxide deactivates significantly during the progression of
7 the redox cycles due to its solid–solid transformation to FeAl_2O_4 , requiring a higher temperature
8 of reduction and reoxidation. Hence, the success of these promoters greatly depends on the
9 nature of these transformations.
10

11
12
13
14
15
16
17
18
19
20 Certain promoters contribute towards the redox reaction, along with iron oxide, in addition to
21 providing a physical barrier. These are therefore termed chemically active promoters, e.g. CeO_2 ,
22 CeZrO_2 ^{16, 27} among the latter, CeO_2 stands out as it has high activity towards methane oxidation
23 by lattice oxygen, as well as reasonable H_2O or CO_2 reoxidation capacity^{28, 29}. The redox couple
24 Ce^{4+} and Ce^{3+} facilitates oxygen storage and release from its bulk fluorite lattice. Additionally,
25 CeO_2 induces structural modification and stabilization of iron oxides, making it an ideal
26 candidate for promoting iron oxide in a chemical looping process. Indeed, the formation of a
27 solid solution between CeO_2 and MeO_x (Me= Mn, Fe, or Cu) has been found to be responsible
28 for enhanced reducibility at lower temperatures compared with pure CeO_2 ⁸.
29

30
31
32
33
34
35
36
37
38
39
40
41 In a previous study, the influence of CeO_2 as chemically active promoter for iron oxides was
42 investigated for a range of loadings. The addition of CeO_2 to Fe_2O_3 resulted in higher activity in
43 comparison to the bulk oxides⁸. Among these mixed oxide materials, 80wt% Fe_2O_3 - CeO_2 showed
44 the highest redox properties. Despite its high initial activity, the material suffered from
45 deactivation, albeit less severe than pure iron oxide. At the opposite side of the Fe_2O_3 - CeO_2
46 mixing range 10wt% Fe_2O_3 - CeO_2 and 30wt% Fe_2O_3 - CeO_2 materials had low oxygen storage
47 capacity but were less prone to deactivation.
48
49
50
51
52
53
54
55
56
57
58
59
60

1
2
3 The present investigation focuses on the origin and nature of deactivation in Fe₂O₃-rich and
4
5 CeO₂-rich Fe₂O₃-CeO₂ materials. For this study, the most active 80wt%Fe₂O₃-CeO₂ was
6
7 compared with 10wt%Fe₂O₃-CeO₂, where CeO₂ acts as bulk oxygen carrier material. The
8
9 addition of a small amount of Fe₂O₃ to CeO₂ is known to result in lower CeO₂ redox
10
11 temperatures, making this material applicable in chemical looping redox processes⁸.
12
13

14
15 Mechanisms of deactivation such as sintering and solid-solid transformation during chemical
16
17 looping were investigated using in situ XRD, TEM and XAS. In situ XRD was employed to
18
19 study the redox properties during the reaction. XAS and TEM were employed to study the local
20
21 environment around Fe and Ce.
22
23
24
25
26

27 **2.0 Experimental**

28 **2.1 Material preparation**

29
30 Fe₂O₃-CeO₂ materials with 10 and 80wt% Fe₂O₃ were prepared. The following chemicals were
31
32 used as precursor materials for the synthesis of mixed oxides: Fe(NO₃)₃·9H₂O (99.99+%, Sigma-
33
34 Aldrich®) and Ce(NO₃)₃·6H₂O(99.99%,Sigma-Aldrich®). All samples were prepared via one
35
36 pot co-precipitation by ammonium hydroxide. The precipitate was then separated by filtration,
37
38 followed by drying in an oven at 120°C for 10 hours. The samples were calcined at 650°C for 6
39
40 hours.
41
42
43
44

45
46 In addition to the above materials, 50wt%Fe₂O₃-CeO₂ was synthesized by co-precipitation and
47
48 subjected to 10 cycles of TPR-TPO up to a temperature of 950°C as pre-treatment. This material
49
50 was used for comparison of perovskite (CeFeO₃) redox properties with cycled materials.
51

52
53 The Brunauer–Emmett–Teller (BET) surface area of each sample was determined by N₂
54
55 adsorption at 77 K (five point BET method using Gemini Micromeritics). Prior to analysis, the
56
57
58
59
60

1
2
3 sample was outgassed at 200 °C for 4 h to eliminate volatile adsorbates from the surface. The
4
5 surface area of as prepared 10 and 80wt%Fe₂O₃-CeO₂ amounted to 18 m²/g and 15 m²/g
6
7 respectively. The surface area of used samples decreased by ten times.
8
9

10 11 12 13 14 **2.2 General characterization: X-Ray Diffraction (XRD)**

15
16 The crystallographic phases of the materials were determined with a Siemens Diffractometer
17
18 Kristalloflex D5000, with Cu K α ($\lambda=0.154\text{nm}$) radiation. The powder patterns were collected in
19
20 a 2θ range from 10° to 80° with a step of 0.02° and 30s counting time per angle. The crystallite
21
22 size was determined using the Scherrer equation by fitting a Gaussian function to the three most
23
24 intense characteristic peaks to obtain the peak width at half maximum.
25
26
27
28
29
30

31 32 **2.3 X-Ray Absorption Spectroscopy (XAS)**

33
34 XAS measurements were performed at the Fe-K (7112 eV), Ce-L_{III} (5873 eV) and Ce-K (40443
35
36 eV) edges. The Fe-K and Ce-L_{III} measurements were performed at the DUBBLE beam line (BM
37
38 26A) and the Ce-K edge data were collected at SNBL (BM 01B) both of the European
39
40 Synchrotron Radiation Facility (ESRF) in Grenoble (France). The optics and energy alignment
41
42 was performed using a Fe foil and CeO₂ reference.
43
44
45
46
47
48

49 50 **2.4 EXAFS data reduction analysis**

51
52 XAS data reduction and analysis were executed with Athena and Artemis, part of the Demeter
53
54 0.9.13 software package³⁰. The pre-edge background was removed by subtracting an
55
56 extrapolated modified Victoreen curve from the raw data. The edge energy E_0 was chosen at the
57
58
59
60

1
2
3 maximum of the first derivative of the spectrum. The atomic background μ_0 was calculated by
4 the AUTOBK routine using a cubic spline fitting procedure. Background subtraction,
5
6 normalization, $\chi(k)$ isolation and Fourier transformation were performed using the methodology
7
8 of Koningsberger et al.³¹. In view of Ce-K edge EXAFS signal modelling, the amplitude
9
10 reduction factor $S_0^2 = 0.83 \pm 0.05$ was calculated from reference CeO₂. The local environment
11
12 of Ce was fitted by implementing a Fe doped CeO₂ model. The single scattering paths with
13
14 significant contribution to the Ce-K signal were selected and used for further modelling.
15
16
17

18
19 The FEFF 6.0 ab initio code³² was applied to calculate the phase shifts and backscattering
20
21 amplitude functions of Ce–O, Ce–Ce and Ce–Fe contributions to the EXAFS signal. IFEFFIT
22
23 was utilized for non-linear least-squares minimization of the objective function using a
24
25 Levenberg–Marquardt algorithm, yielding estimates for the structural parameters³⁰. For this
26
27 minimization, multiple shell fitting was performed in R-space using multiple k-weightings. The
28
29 fitting was performed by model discrimination of fit by implementing single scattering paths
30
31 with and without incorporation of Fe. The agreement between model and experiment was
32
33 evaluated statistically by means of the minimized objective function χ_ν^2 and the F-value. The χ_ν^2
34
35 is the reduced sum of square residuals with ν degrees of freedom. The F-test was performed
36
37 using Hamiltonian formulation³³ and the confidence interval α was calculated by the approach
38
39 described by Bacchi et al.³⁴. For global significance of the regression the inverse F-value or R-
40
41 value is reported.
42
43
44
45
46
47
48

49 **2.5 In situ XRD analysis**

50
51 The crystallographic changes during H₂-TPR and CO₂-TPO were followed with in situ XRD in a
52
53 home-built reaction chamber housed inside a Bruker-AXS D8 Discover apparatus (Cu K α
54
55 radiation of 0.154 nm) with a linear detector covering 20° in 2 θ and an angular resolution of
56
57
58
59
60

1
2
3 approximately 0.1° in 2θ . A typical collection time of 10 s was used during these experiments.
4
5
6 10 mg of powdered sample was evenly spread on a single crystal Si wafer. Interaction of the
7
8 catalyst material with the Si wafer was never observed. After pump-down to a base pressure of 4
9
10 Pa, gases were supplied to the reactor chamber from a rig with calibrated mass flow meters.
11
12 A full XRD scan (10° to 65° with a step of 0.02°) was recorded at room temperature before and
13
14 after each TPR and TPO experiment. The TPR was performed in flow conditions of H_2 at
15
16 1.1Nml/sec up to a temperature of $800^\circ C$. This was followed by reoxidation with CO_2 at the
17
18 same flow rate up to $800^\circ C$. Both of these treatments were performed at a uniform heating rate of
19
20 $20^\circ C/min$.
21
22
23

24 25 26 **2.6 TEM**

27
28 High angle annular dark field scanning transmission electron microscopy (HAADF-STEM),
29
30 energy dispersive X-ray (EDX) spectroscopy and electron energy-loss spectroscopy (EELS)
31
32 experiments were performed with a FEI Titan “cubed” electron microscope equipped with an
33
34 aberration corrector for the probe-forming lens, a high resolution EELS spectrometer (Gatan GIF
35
36 Quantum) and a wide solid angle “super-X” EDX detector, at 120 kV and 300 kV acceleration
37
38 voltage. The STEM convergence semi-angle used was ~ 22 mrad, while the inner collection
39
40 semi-angle for HAADF-STEM imaging at 300kV was ~ 50 mrad and at 120kV ~ 85 mrad.
41
42
43
44

45 46 **2.7 Experimental Reactor Setup**

47
48 Redox cycling measurements were carried out at atmospheric pressure in a quartz tube
49
50 microreactor (i.d. 10 mm), placed in an electric furnace. Typically, 30 mg of material was packed
51
52 in a quartz bed. This material was diluted with inert $\alpha-Al_2O_3$ with a ratio of 1:10. The
53
54 temperature of the catalyst bed was measured with K-type thermocouples touching the outside
55
56 and inside of the reactor at the position of the catalyst bed. In all experiments, the material was
57
58
59
60

1
2
3 reduced by H₂ and reoxidized by CO₂. In between He was purged during redox cyclic
4 experiments. The total flow rate of the feed gas into the reactor was maintained constant at
5
6 1.1Nml/s by means of Brooks mass flow controllers. The redox property of the samples was
7 investigated at 650°C. The feed and product gas streams were monitored online using an
8
9 OmniStar Pfeiffer mass spectrometer (MS). The response of the MS detector was regularly
10
11 verified with calibration gases. A carbon balance with a maximum deviation of 15% was
12
13 obtained. The CO yield is calculated as (equation 1)
14
15
16
17
18

$$\text{Yield } (Y_i) = \frac{n_{CO}}{W} \quad (\text{Eq. 1})$$

19
20 where n_{CO} = Mole of CO produced (mol) ; W_{Fe} = Mass of oxygen carrier material [kg].
21
22
23
24
25

26 **3.0 Results**

27 **3.1 Isothermal Cycling**

28
29 The effect of redox cycling on the CO yield of 80wt%Fe₂O₃-CeO₂ and 10wt%Fe₂O₃-CeO₂ was
30
31 studied at a temperature of 650°C during 100 redox cycles (Figure 1). The highest CO yield was
32
33 shown by 80wt%Fe₂O₃-CeO₂. In this material the CO yield decreased steadily during the first 30
34
35 cycles and thereafter remained stable. For 10wt%Fe₂O₃-CeO₂, the CO yield steeply dropped
36
37 during the first 10 cycles and then remained constant up to 100 cycles. Over the redox cycles, the
38
39 conversion of CO₂ decreased from 15% to 6% for 80Fe-CeO₂ and from 9% to 2% for 10Fe-
40
41 CeO₂. This decrease in CO yield for both materials is the result of deactivation. However, the
42
43 different trends in decrease of CO yield (Figure 1) could suggest that different factors could
44
45 govern the deactivation, determined by the interaction between the metal oxides present in both
46
47 oxygen storage materials¹³, possibly leading to different routes of deactivation. In order to
48
49 identify the different mechanisms of deactivation, a systematic characterization of materials was
50
51 performed to map out their redox properties in relation to their stability.
52
53
54
55
56
57
58
59
60

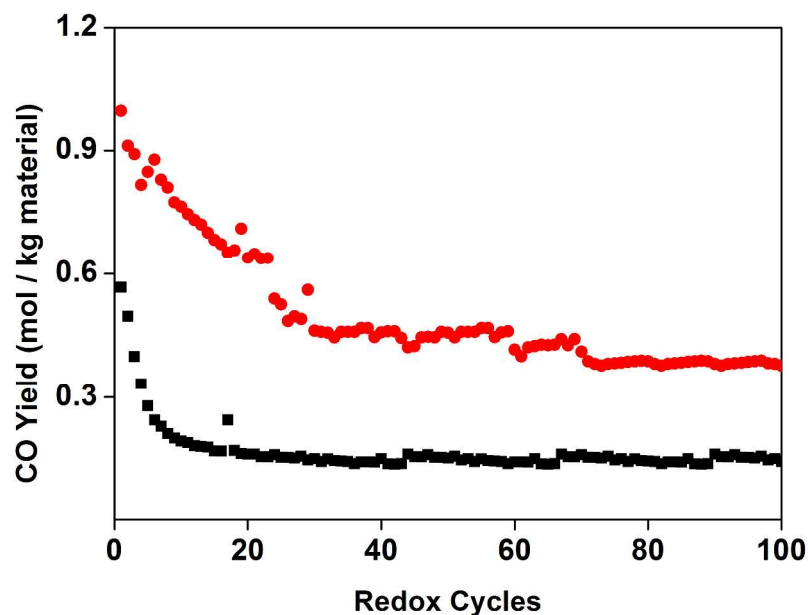


Figure 1: CO yield as a function of number of isothermal redox cycles for 10wt%Fe₂O₃-CeO₂ and 80wt%Fe₂O₃-CeO₂. (●) 80wt%Fe₂O₃-CeO₂ and (■) 10wt%Fe₂O₃-CeO₂.

3.2 Materials Characterization

3.2.1 XRD

The as prepared and cycled materials were characterized using XRD to identify the phases present. From the diffraction pattern of 80wt%Fe₂O₃-CeO₂ (Figure 2a (i)), characteristic peaks for Fe₂O₃ and CeO₂ were identified. For 10wt%Fe₂O₃-CeO₂ clear contributions of CeO₂ along with minor peaks of Fe₂O₃ (dotted lines) were observed (Figure 2a (ii)).

The state of the materials after redox cycling is shown in Figure 2b. The diffraction pattern of cycled 80wt%Fe₂O₃-CeO₂ (Figure 2b(i)) exhibited peaks at 2θ values corresponding to CeO₂ and Fe₃O₄. From the XRD of cycled 10wt%Fe₂O₃-CeO₂ (Figure 2b(ii)), peaks of CeO₂, Fe₃O₄ and

1
2
3 perovskite (CeFeO_3) as new phase were identified. Further reoxidation to Fe_2O_3 can only be
4
5 achieved if O_2/air is employed for reoxidation³⁵.
6
7

8 The crystallite sizes of the as prepared materials and 100 times cycled materials were calculated
9
10 using the Scherrer equation (Table 1). For Fe_2O_3 in as prepared 80wt% Fe_2O_3 - CeO_2 and Fe_3O_4 in
11
12 both cycled materials, reliable values could be obtained from XRD. However, in as prepared
13
14 10wt% Fe_2O_3 - CeO_2 the Fe_2O_3 diffractions were too weak for crystallite size determination.
15
16 Hence, for the Fe_2O_3 phase in this material, crystallite sizes from TEM are reported in Table 1.
17
18 The crystallite size of CeO_2 determined by XRD showed that crystallites in 10wt% Fe_2O_3 - CeO_2
19
20 are larger than in 80wt% Fe_2O_3 - CeO_2 . In addition, the formation of a solid solution $\text{Ce}_{1-x}\text{Fe}_x\text{O}_{2-x}$
21
22 was identified from the lattice parameters of CeO_2 for both as prepared 10wt% Fe_2O_3 - CeO_2 and
23
24 80wt% Fe_2O_3 - CeO_2 (Table 1). The replacement of a larger cation (Ce^{+4} , 1.01 Å) with a smaller
25
26 one (Fe^{+3} , 0.64 Å) led to contraction of the lattice and, hence, a smaller lattice parameter in
27
28 comparison to pure CeO_2 (0.5411 nm)⁸. This is in agreement with the CeO_2 lattice parameter
29
30 evolution for a series of 2wt% to 80wt% Fe_2O_3 - CeO_2 (details of lattice parameter evolution for
31
32 the series of materials in supplementary info Figure S1) and suggests that during synthesis,
33
34 incorporation of Fe in CeO_2 occurred to form a solid solution $\text{Ce}_{1-x}\text{Fe}_x\text{O}_{2-x}$ which stabilized the
35
36 crystallite size of CeO_2 . The resulting solid solutions $\text{Ce}_{1-x}\text{Fe}_x\text{O}_{2-x}$ in both 10wt% Fe_2O_3 - CeO_2
37
38 and 80wt% Fe_2O_3 - CeO_2 are expected to present enhanced redox properties compared to pure
39
40 CeO_2 ¹⁶.
41
42
43
44
45
46
47
48
49
50
51
52
53
54
55
56
57
58
59
60

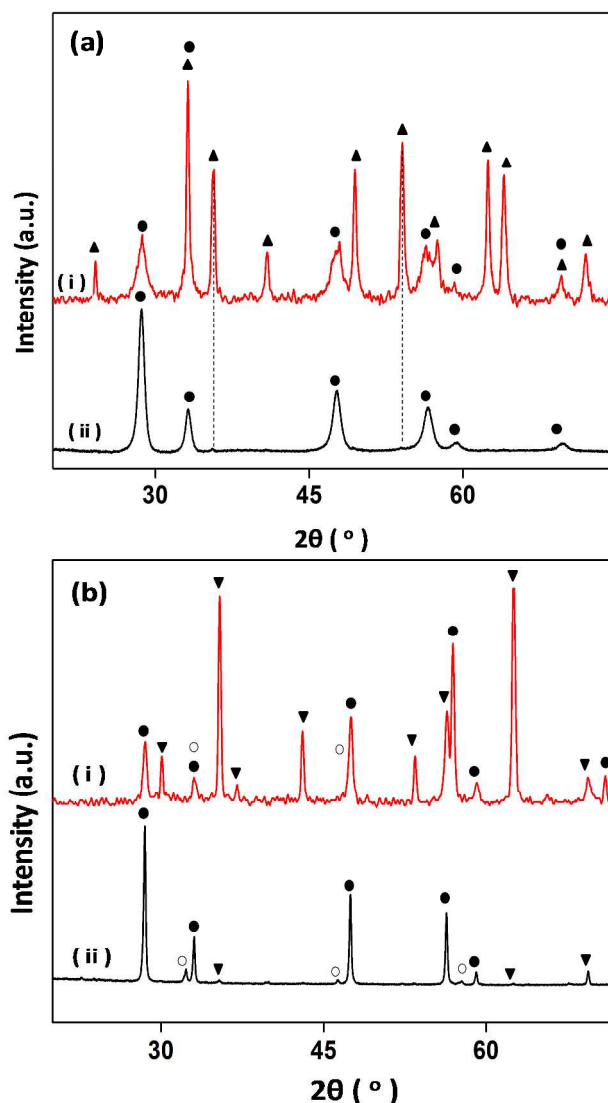


Figure 2: XRD diffraction patterns of (i) 80wt%Fe₂O₃-CeO₂ and (ii) 10wt%Fe₂O₃-CeO₂: a) as prepared and (b) 100 times cycled. (▲) Fe₂O₃, (●) CeO₂, (▼) Fe₃O₄, and (○) CeFeO₃.

After cycling, CeO₂ crystallites showed a 2.5 times increase in 10wt%Fe₂O₃-CeO₂ and 4 times increase in 80wt%Fe₂O₃-CeO₂. This was due to sintering of the oxygen storage material and segregation of incorporated Fe from the CeO₂ lattice, resulting in the formation of separate Fe₃O₄ phase. This phase segregation is also evidenced from the CeO₂ lattice parameters of cycled materials (Table 1) which were closer to that of pure CeO₂ (0.5411 nm), which indicates that part of the Fe was segregated upon cycling, leaving less Fe incorporated in the CeO₂ lattice.

Further, the new perovskite phase CeFeO_3 formed in $10\text{wt}\%\text{Fe}_2\text{O}_3\text{-CeO}_2$ upon cycling, also displayed large crystallite sizes (Table 1). Crystallites of pure iron oxide also suffered from heavy sintering. In $80\text{wt}\%\text{Fe}_2\text{O}_3\text{-CeO}_2$ the increase was only twofold, which could be due to CeO_2 nanocrystallites acting as a physical barrier and thereby controlling the sintering of iron oxides. The increase of crystallite size was more predominant in $10\text{wt}\%\text{Fe}_2\text{O}_3\text{-CeO}_2$, where sintering yielded a tenfold increase of the iron oxide crystallite size.

Table 1: Crystallite sizes and CeO_2 lattice parameters of as prepared and cycled materials from XRD.

Phase	$10\text{wt}\%\text{Fe}_2\text{O}_3\text{-CeO}_2$		$80\text{wt}\%\text{Fe}_2\text{O}_3\text{-CeO}_2$	
	Fresh (nm)	100 cycles (nm)	Fresh (nm)	100 cycles (nm)
CeO_2	15 ± 3	38 ± 4	9 ± 3	35 ± 4
CeFeO_3	b	75 ± 10	b	b
$\text{Fe}_2\text{O}_3/\text{Fe}_3\text{O}_4$	$5^{\text{a,b}}$	48 ± 13	54 ± 4	98 ± 6
Lattice parameter from $\text{CeO}_2(111)$	0.5385 ± 0.0005	0.5401 ± 0.0007	0.5389 ± 0.0004	0.5401 ± 0.0005

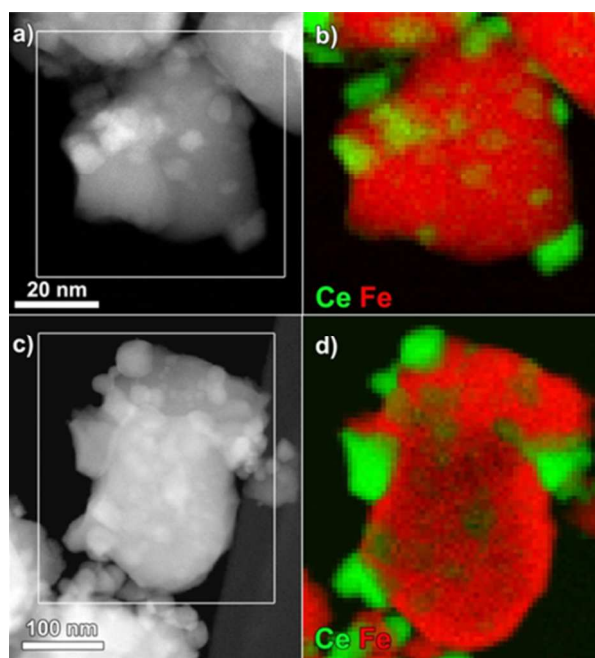
^a-determined from TEM, ^b- no diffraction peaks present. Error represents standard deviation calculated from 3 most intense peaks.

3.2.2 TEM

The HAADF-STEM image of the as prepared $80\text{wt}\%\text{Fe}_2\text{O}_3\text{-CeO}_2$ sample (Figure 3a) demonstrates the presence of two kinds of particles. The smaller nanoparticles were identified as CeO_2 based on the EELS mapping (Figure 3b). They decorated the larger crystallites of Fe_2O_3 (~50nm). Strong agglomeration of the nanoparticles during cycling (for 100 cycles) led to a significant change of the particle size (Figure 3c). However, the sintered particles of ceria and iron oxide still demonstrate a similar proportion as in the as prepared situation where smaller

1
2
3 ceria nanoparticles decorate the larger iron oxide nanoparticles (Figure 3d). The size of the
4
5 nanoparticles observed after cycling is in agreement with the size retrieved based on XRD data.
6
7

8 The HAADF-STEM image of the as prepared 10wt%Fe₂O₃-CeO₂ (Figure 4a) demonstrates the
9
10 nanoparticulate morphology of the sample. Elemental mapping (Figure 4b) shows mainly ceria
11
12 particles to be present. After cycling, the material remains nanosized (Figure 4c), consisting
13
14 mainly of ceria nanoparticles (Figure 4d). However, several dispersed iron oxide nanoparticles
15
16 are observed as well. The crystallite sizes calculated from TEM were in agreement with XRD
17
18 from Table 1.
19
20
21



44 **Figure 3:** a) HAADF-STEM image of the as prepared 80wt%Fe₂O₃-CeO₂ sample; b)
45 corresponding EELS map for Fe and Ce; c) HAADF-STEM image of the 100 times cycled
46 80wt%Fe₂O₃-CeO₂ sample; d) corresponding EELS map for Fe and Ce.
47
48
49
50
51
52
53
54
55
56
57
58
59
60

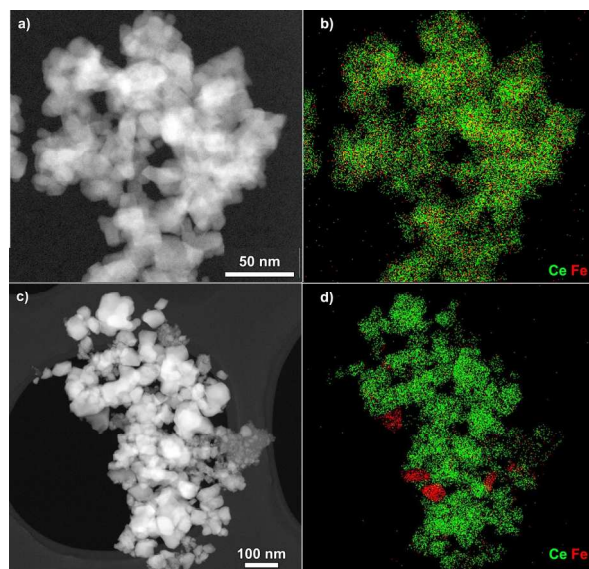


Figure 4: a) HAADF-STEM overview of as prepared 10wt%Fe₂O₃-CeO₂ with b) corresponding EDX map for Ce and Fe. c) HAADF-STEM overview of the 100 times cycled 10wt%Fe₂O₃-CeO₂ sample together with d) corresponding EDX map for Ce and Fe.

3.2.3 XAS: *Structural Modeling*

The incorporation of Fe inside CeO₂ lattice resulted in the formation of solid solution Ce_{1-x}Fe_xO_{2-x} as evidenced from the XRD lattice parameters for CeO₂. The lattice parameter evolution of CeO₂ over a range (2-80wt%Fe₂O₃-CeO₂) of mixed oxide materials (Supplementary Figure S1) shows a plateau between 10wt% and 80wt%Fe₂O₃-CeO₂. This indicates that for each of these materials a similar amount of Fe is incorporated inside the CeO₂ lattice. In addition, in the XRD patterns (Figure 2a (ii)) no major contribution of Fe₂O₃ in 10wt%Fe₂O₃-CeO₂ was present, indicating that a large fraction of Fe can be incorporated inside the CeO₂ lattice. In order to obtain a value for the amount of Fe inside the CeO₂ lattice in as prepared materials, structural modeling was applied to the Ce-K edge EXAFS data. Hence, to determine the amount of Fe dissolved inside the CeO₂ lattice, modeling of 10wt%Fe₂O₃-CeO₂ was pursued at the Ce-K edge. The model was implemented by comparing the CeO₂ fluorite structure and a Fe doped CeO₂

fluorite structure, denoted as $Ce_{1-x}Fe_xO_{2-x}$ where x is the amount of dissolved Fe as parameter to be determined. Both models were fit to the Ce-K EXAFS signal of 10wt% Fe_2O_3 - CeO_2 at ambient conditions ($\Delta k = 0.24$ – 1.01 nm^{-1} , $\Delta R = 0.13$ – 0.41 nm). The fit using the Fe doped CeO_2 structure yielded an R -value of 0.0034, whereas for the fit using the pure CeO_2 structure an R -value of 0.0064 was obtained. The F test was performed, generating a confidence level α of 94% for the hypothesis that the Fe doped CeO_2 structural model yielded a significantly better fit than the pure CeO_2 model. Consequently, pure CeO_2 was rejected as structural model and thus, the model with Fe doped CeO_2 was chosen as best representing the Fe-doped CeO_2 lattice.

Table 2: Fit results of the Fe incorporated CeO_2 model ($\Delta k = 0.24$ – 1.01 nm^{-1} , $\Delta R = 0.13$ – 0.41 nm) in R-space with multiple k_i -weighted ($i = 1, 2$ and 3) to the Ce-K edge EXAFS signal of 10wt% Fe_2O_3 - CeO_2 in ambient conditions.

	R (Å)	N	σ^2 (Å²)
Ce-O	2.341±0.001	7.61±0.70	0.0078±0.0012
Ce-Ce	3.824±0.002	9.39±2.26	0.0047±0.0016
Ce-Fe	3.843±0.016	2.89±1.20	0.0047±0.0016
Ce-O	4.484±0.002	27±20.12	0.0171±0.0117

The regression fit results of Fe doped CeO_2 are shown in Table 2. The coordination of the first shell remains close to that of pure CeO_2 . However, the second shell is split into contributions of Ce and Fe. In order to decorrelate the coordination number N of Fe scatterers in the second shell around the Ce absorber from the Debye–Waller factor for these Fe atoms, the latter was kept equal to the one of the Ce atoms. The Debye–Waller factor of the first Ce-O shell showed a high value, because oxygen as lighter element exhibits a higher entropy. An increase in Debye–Waller

factor was also observed in the next O shell due to the light O scatterers and to the Fe incorporation into the lattice of CeO_2 . A best fit (Figure 5) was obtained with $x = 0.21 \pm 0.08$ so that 21% of the Ce atoms in CeO_2 is substituted with Fe. This corresponds to 85% of the Fe available, residing within the $\text{Ce}_{1-x}\text{Fe}_x\text{O}_{2-x}$ solid solution in 10wt% Fe_2O_3 - CeO_2 . For 80wt% Fe_2O_3 - CeO_2 , it can be assumed that the same amount of Ce is replaced with Fe, i.e. 21mol%, based on the similar CeO_2 lattice parameters. This will of course represent a much smaller fraction of Fe in 80wt% Fe_2O_3 - CeO_2 than in 10wt% Fe_2O_3 - CeO_2 .

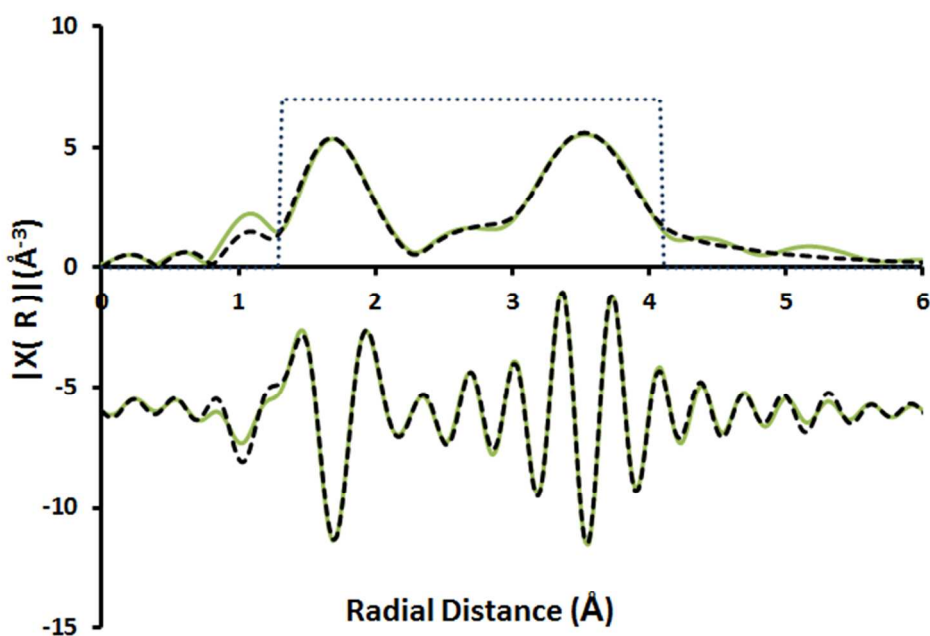


Figure 5: Fourier transformed k^2 -weighted EXAFS signal of 10wt% Fe_2O_3 - CeO_2 and k_i -weighted ($i = 1, 2$ and 3) fit (dashed line) with Fe incorporated CeO_2 model $\text{Ce}_{1-x}\text{Fe}_x\text{O}_{2-x}$ and $x = 0.21$. The upper part represents the modulus of FT, whereas the lower part is the imaginary part $\text{Im}[\text{FT}\{k^2 \chi(R)\}]$. The dotted rectangle indicates the window fitting range. No phase correction was used. (—) EXAFS signal of 10wt% Fe_2O_3 - CeO_2 , (---) fit and (.....) fitting window.

3.2.4 In situ characterization: Solid-solid transformation

The material transformations affecting the redox properties during prolonged cycling were investigated during H₂-TPR and CO₂-TPO using in situ XRD³⁶⁻³⁹ and conventional temperature-programmed reaction. The crystallographic changes observed in in situ XRD were correlated with the consumption profiles from the conventional temperature-programmed experiments.

3.2.4.1 H₂-TPR

3.2.4.1a 80wt %Fe₂O₃-CeO₂

Figure 6a represents the crystallographic changes during H₂-TPR of as prepared 80wt%Fe₂O₃-CeO₂. The transition of Fe₂O₃ to Fe₃O₄ occurs at a temperature of ~450°C and further transformation of Fe₃O₄ to FeO starts around ~500°C. The deeper reduction of FeO to Fe is identified by the appearance of the diffraction peak of metallic Fe at 2θ=45° at higher temperature ~600°C. Diffraction peaks for CeO₂ (111) and (200) at 2θ=28° and 33° were observed without an apparent phase transformation to Ce₂O₃. This is in agreement with the bulk reduction from CeO₂ to Ce₂O₃ occurring at a much higher temperature⁴⁰. After redox cycling of this material, Fe₃O₄ and CeO₂ are the major phases detected by in situ XRD (Figure 6b). A H₂-TPR of the cycled material shows a faint transition from Fe₃O₄ to FeO at ~500°C, temperature at which also the deeper reduction to metallic Fe starts. The temperature, at which successive reductions occur for both states of the 80wt%Fe₂O₃-CeO₂ sample, was further evaluated based on the diffraction intensity variations segregated from the in situ XRD map (Figure 6c). All phase transitions occur at similar temperature for the as prepared and cycled material.

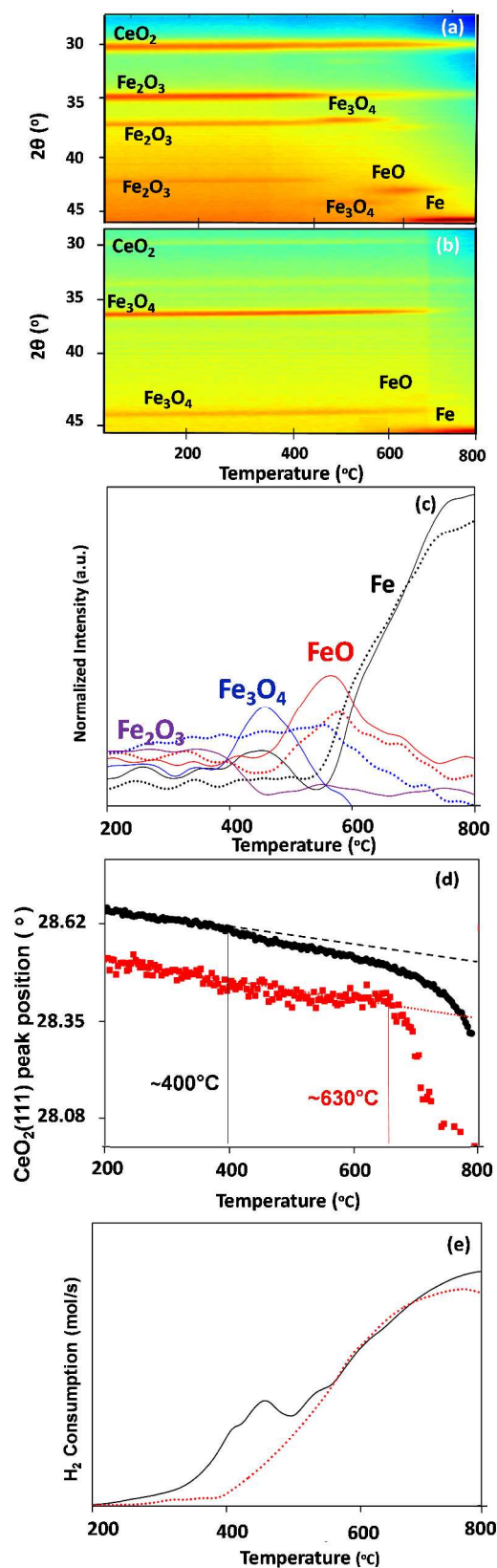


Figure 6: Evolution of 80wt%Fe₂O₃-CeO₂ during H₂-TPR as followed by in situ XRD and conventional TPR. Crystallographic changes of 80wt%Fe₂O₃-CeO₂ in (a) as prepared and (b) 100 times cycled sample; (c) intensity variation of iron oxide phases from in situ XRD in (a) and (b); Intensity changes during in situ XRD of (—) as prepared, (.....) 100 times cycled sample; (d) changes in CeO₂ (111) position of as prepared and 100 cycled material; Variation of CeO₂ (111) peak position with temperature for (●) as prepared and (■) 100 times cycled sample; dotted and dashed lines represent thermal lattice expansion; (e) H₂ consumption profiles during conventional -TPR of (—) as prepared, (.....) 100 times cycled sample.

1
2
3 Parallel to iron oxide reduction, CeO_2 could also take part in the reduction, even if no true phase
4 transition takes place. This was verified by following the CeO_2 (111) peak position as a function
5 of temperature (Figure 6d). Thermal lattice expansion induces a gradual lowering of the peak
6 position, indicated by the dashed lines. However, deviations from the extrapolated thermal
7 expansion occur at 400°C for as prepared material, indicating a stronger increase of the lattice
8 size. This is due to partial reduction of the lattice, since Ce^{3+} is larger than Ce^{4+} , which causes an
9 abrupt shift to lower 2θ values at this temperature. For the cycled material, no downward
10 deviation was observed. As indicated by the lattice parameters from XRD (Table 1), the cycling
11 already segregates Fe from the solid solution, which could make the remaining phase less prone
12 to partial reduction. Above 700°C , bulk reduction of CeO_2 sets in, accompanied by a further
13 lattice expansion.
14
15
16
17
18
19
20
21
22
23
24
25
26
27
28

29 Based on the analysis of in situ XRD, the conventional H_2 -TPR profiles can be interpreted in
30 terms of reduction of iron and cerium oxide phases. In Figure 6e a sharp consumption peak at
31 $\sim 450^\circ\text{C}$ is observed for the as prepared material followed by a broad peak around 700°C . Based
32 on in situ XRD (Figure 6a), the consumption peak at $\sim 450^\circ\text{C}$ refers to the transition of Fe_2O_3 to
33 Fe_3O_4 together with the partial reduction of CeO_2 (Figure 6d), which contributes to the onset of
34 the conventional reduction profile. Further reduction from Fe_3O_4 to FeO and FeO to Fe are
35 established within the high temperature single broad peak, together with the start of bulk CeO_2
36 reduction above 700°C . For the 100 times cycled sample, the single broad peak in the reduction
37 profile corresponds to the simultaneous reduction of Fe_3O_4 to FeO, of FeO to metallic Fe (Figure
38 6c) and the onset of CeO_2 bulk reduction above 650°C (Figure 6d).
39
40
41
42
43
44
45
46
47
48
49
50
51
52

53 Overall, the complete reduction of Fe_3O_4 to Fe occurs at a relatively higher temperature for the
54 cycled sample than for the as prepared one, due to increased particle size (Table 1). For the
55
56
57
58
59
60

1
2
3 partial reduction of CeO_2 , the opposite was true. The latter can be understood since cycling
4
5 results in partial Fe segregation, as evidenced from the increased CeO_2 lattice parameter (Table
6
7
8 1), leading to decreased redox properties.
9

10 **3.2.4.1b 10wt % Fe_2O_3 - CeO_2**

11
12 A similar in situ XRD analysis was performed on 10wt% Fe_2O_3 - CeO_2 to examine the change in
13
14 reducibility of the as prepared and cycled material. While diffraction peaks of Fe_2O_3 were not
15
16 observed during the in situ XRD of as prepared material (Figure 7a), metallic Fe appeared above
17
18 $\sim 600^\circ\text{C}$. For the cycled material, the phases of CeO_2 , perovskite (CeFeO_3) and Fe_3O_4 were
19
20 identified in the sample at the start of TPR (Figure 7b). Reduction to metallic Fe started at a
21
22 temperature of $\sim 550^\circ\text{C}$. The diffraction peaks of perovskite (CeFeO_3) and CeO_2 remain visible
23
24 throughout reduction and no peaks corresponding to Ce_2O_3 were observed.
25
26
27

28
29 The transition temperature to Fe in as prepared and cycled materials was further evaluated using
30
31 the integrated diffraction intensities. The intensity plot versus temperature (Figure 7c) shows the
32
33 onset of formation of metallic Fe in the as prepared sample already starting at $\sim 400^\circ\text{C}$. For the
34
35 cycled sample, the formation of metallic Fe is observed around 600°C when Fe_3O_4 is almost
36
37 completely consumed (Figure 7c). The late onset of reduction of Fe is the result of sintering
38
39 which leads to an increased crystallite size (Table 1). The latter results in higher reduction
40
41 temperatures due to a prolonged diffusion time of oxygen from bulk to surface. The reduction to
42
43 metallic Fe in the cycled sample shifts upward by 200°C , unlike in 80wt% Fe_2O_3 - CeO_2 where the
44
45 reduction to metallic Fe was observed at a similar temperature in the cycled sample. As cycling
46
47 leads to sintering as evidenced by the crystallite size increase (Table 1) and to formation of
48
49 perovskite (CeFeO_3), these phenomena must be held responsible for the higher reduction
50
51 temperature of cycled 10wt% Fe_2O_3 - CeO_2 .
52
53
54
55
56
57
58
59
60

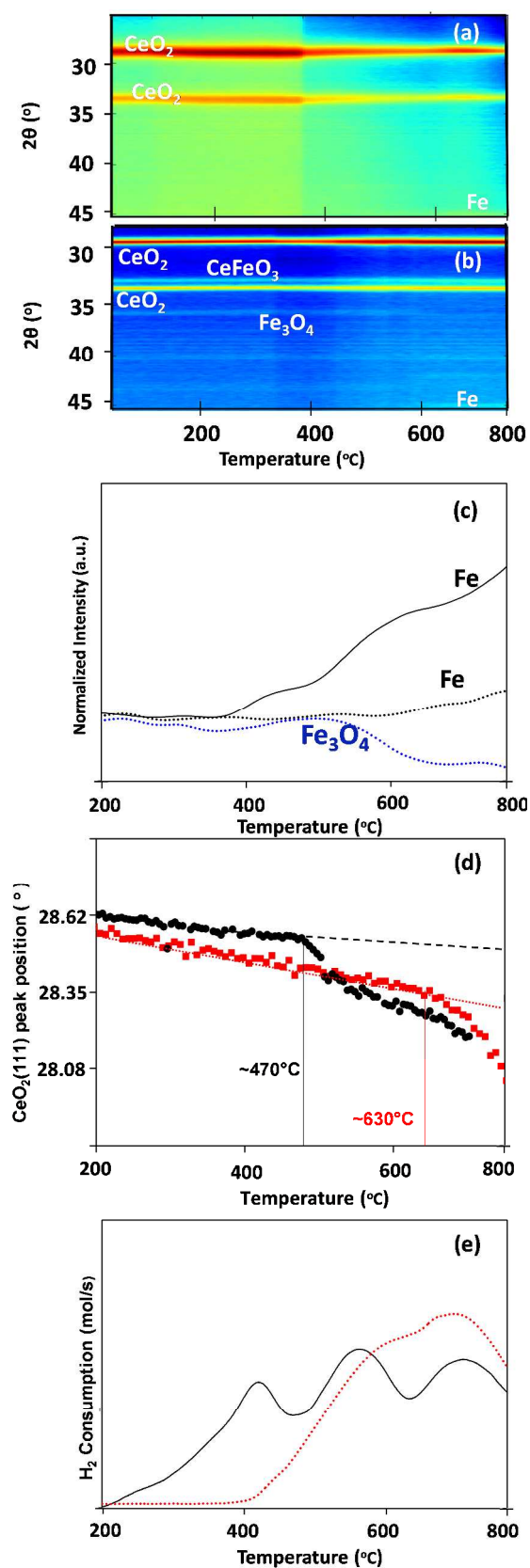


Figure 7: Evolution of 10wt%Fe₂O₃-CeO₂ during H₂-TPR as followed by in situ XRD and conventional TPR: crystallographic changes of (a) as prepared and (b) 100 times cycled sample; Variations of iron oxide diffractions during in situ XRD of (—) as prepared, (.....) 100 times cycled sample; (c) intensity variation of iron oxide phases from in situ XRD; (d) changes in CeO₂ (111) position of as prepared and cycled material; Changes of CeO₂ (111) peak position with temperature for (●) as prepared and (■) 100 times cycled sample; dotted and dashed lines represent thermal lattice expansion; (e) H₂ consumption profiles during H₂ (—) as prepared, (.....) 100 times cycled material.

Possible reduction of CeO_2 was accessed as before from a peak position analysis (Figure 7d). In as prepared material partial reduction of CeO_2 is seen at $\sim 450^\circ\text{C}$, while in the cycled sample it hardly occurred before bulk reduction started. The early reduction in the as prepared materials is ascribed to the enhanced reducibility of CeO_2 species promoted by incorporated Fe.

Using the above results from in situ XRD, the conventional H_2 -TPR on as prepared and cycled $10\text{wt}\%\text{Fe}_2\text{O}_3\text{-CeO}_2$ were interpreted. The consumption profile for as prepared material shows three peaks (Figure 7e). The first peak at $\sim 425^\circ\text{C}$ can be ascribed to reduction of Fe_2O_3 to Fe_3O_4 as also seen in $80\text{wt}\%\text{Fe}_2\text{O}_3\text{-CeO}_2$, although this transition remained invisible in in situ XRD. The second peak $\sim 550^\circ\text{C}$ could correspond to the early reduction of the Ce^{+4} species promoted by Fe and first reduction to metallic Fe. The third peak follows from reduction to metallic Fe and bulk CeO_2 reduction. For the cycled sample, a single broad H_2 consumption peak is observed arising from the onset of bulk CeO_2 reduction, with a shoulder on the rising edge, originating from iron oxide reduction to metallic Fe.

3.2.4.2 CO_2 -TPO

The in situ H_2 -TPR was followed by CO_2 -reoxidation for all samples. The reoxidation temperatures for partially reduced CeO_2 were evaluated as before from the CeO_2 (111) peak position, and compared with conventional TPO temperatures (Figure 8). The profile of reoxidation for as prepared $10\text{wt}\%\text{Fe}_2\text{O}_3\text{-CeO}_2$ material after reduction (Figure 8a) first peaked at 400°C with the bulk reoxidation occurring at 500°C , whereas that of the 100 times cycled sample appeared in a single peak at 600°C . The CO_2 consumption peak of as prepared material at 400°C corresponds to reoxidation of the solid solution $\text{Ce}_{1-x}\text{Fe}_x\text{O}_{2-x}$, based on the CeO_2 (111) peak position change from in situ XRD (Figure 8b). The second peak corresponds to reoxidation of metallic Fe to Fe_3O_4 , which starts at 500°C (Supplementary info Figure S2a) and further

reoxidation of Ce^{+3} . For the 100 times cycled sample, the single broad consumption curve represents the combined reoxidation of Ce^{+3} above 450°C and metallic Fe from 550°C on (Figure 8b and supplementary info Figure S2b).

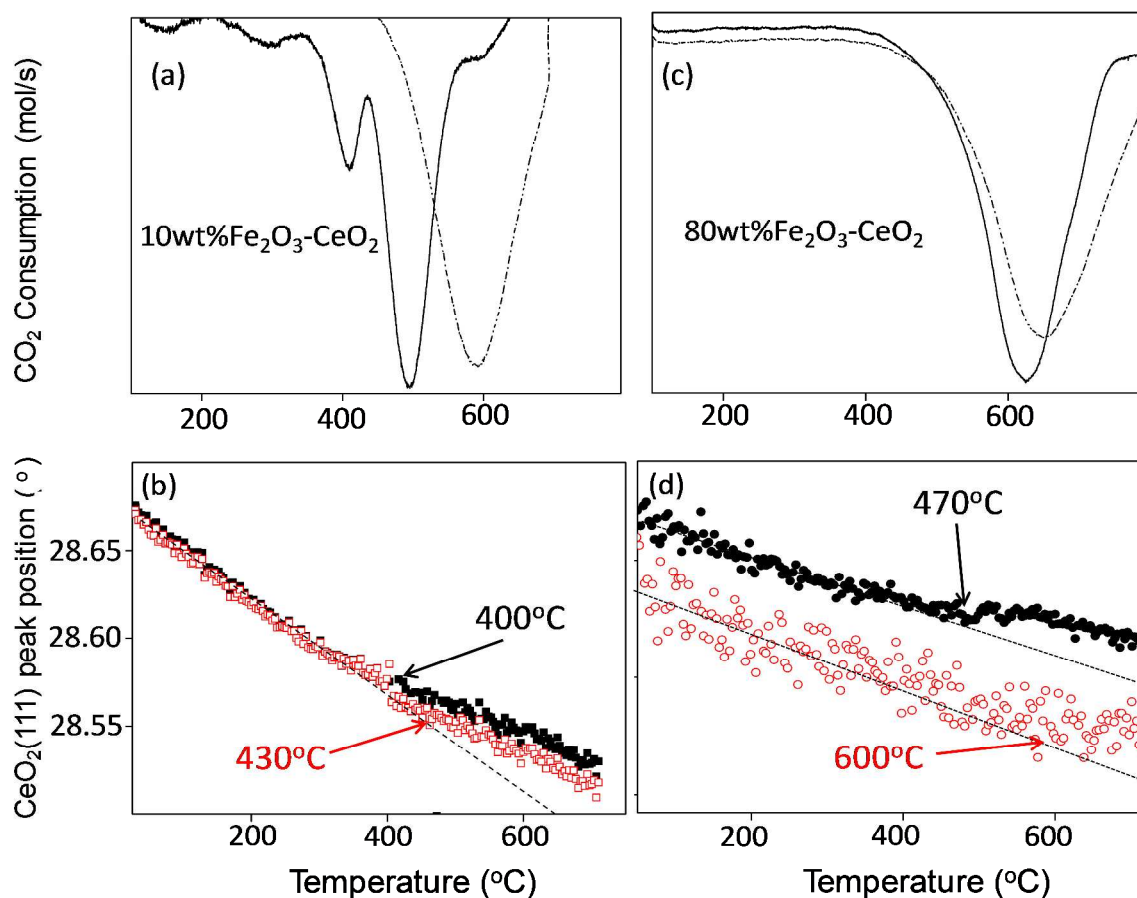


Figure 8: conventional reoxidation profiles of (a) 10wt%Fe₂O₃-CeO₂ and (c) 80wt% Fe₂O₃-CeO₂, as prepared and 100 cycled; changes in the CeO₂ (111) peak position during CO₂ reoxidation of (b) 10wt%Fe₂O₃-CeO₂ and (d) 80wt% Fe₂O₃-CeO₂, as prepared and 100 times cycled. Consumption profiles during conventional CO₂-TPO of (—) As prepared, (---) 100 times cycled sample. CeO₂ peak position of 10wt%Fe₂O₃-CeO₂ (■) as prepared, (□) 100 times cycled and 80wt%Fe₂O₃-CeO₂ (●) as prepared and (○) 100 times cycled sample. Each cycle (16 min) is composed of 4 min H₂ (5% in Ar), 4 min He, 4 min CO₂ (100%) and 4 min He at 650°C . All the gas flows were 1.1 Nml/s.

1
2
3 A similar analysis was performed for 80wt%Fe₂O₃-CeO₂. The reoxidation of as prepared and
4
5
6 cycled materials of 80wt%Fe₂O₃-CeO₂ (Figure 8c) peaked at similar temperatures (~600°C). The
7
8 position analysis of CeO₂(111) shows that partial reoxidation of Ce⁺³ to Ce⁺⁴ occurs at ~470°C
9
10 for as prepared material and at ~600°C for the 100 times cycled sample (Figure 8d). These
11
12 temperatures fall within the conventional reoxidation profile of both materials. In addition, these
13
14 broad peaks contain a contribution from the reoxidation of metallic Fe to Fe₃O₄, occurring at
15
16 400°C for as prepared and at 350°C for cycled material (Supplementary info Figure S3a&b).
17
18 Similar reoxidation temperatures were observed in the fresh and cycled samples for
19
20 80wt%Fe₂O₃-CeO₂, whereas in 10wt%Fe₂O₃-CeO₂ the reoxidation of the cycled sample shifted
21
22 to higher temperatures.
23
24
25
26
27
28
29

30 **4.0 Discussion**

31
32 In chemical looping, deactivation of Fe₂O₃-CeO₂ oxygen storage materials is observed as a
33
34 decline in CO yield as a function of redox cycles. Extensive characterization of materials, by
35
36 means of In situ XRD, TEM and XAS, showed the latter is due to a combination of solid-solid
37
38 transformation and sintering. The former comprises the formation of a new phase and/or
39
40 elemental segregation. Sintering on the other hand leads to an increase of crystallite size and,
41
42 hence, smaller surface area. The nature and extent of these changes determine the overall yield of
43
44 the chemical looping reaction in a prolonged redox process.
45
46
47
48

49 **4.1 Solid-solid transformation**

50
51 The first kind of deactivation is due to strong promoter and support interaction during prolonged
52
53 redox cycling. For the materials of the present study, solid-solid transformation can be
54
55 categorized into two types: 1) formation of a perovskite phase CeFeO₃ due to interaction of Fe
56
57
58
59
60

1
2
3 and CeO₂ during redox cycling⁴¹⁻⁴⁴ and 2) segregation of Fe from the solid solution Ce_{1-x}Fe_xO_{2-x}.
4
5
6
7
8
9
10
11
12
13
14
15
16
17
18
19
20
21
22
23
24
25
26
27
28
29
30
31
32
33
34
35
36
37
38
39
40
41
42
43
44
45
46
47
48
49
50
51
52
53
54
55
56
57
58
59
60

and CeO₂ during redox cycling⁴¹⁻⁴⁴ and 2) segregation of Fe from the solid solution Ce_{1-x}Fe_xO_{2-x}.²³. The perovskite formation was identified using in situ XRD and XAS, while the segregation of Fe was identified using the XRD lattice parameter evolution during the first 10 cycles.

In the first type of deactivation, the amount of exchangeable oxygen is restricted by the nature of the phase formed. If the new phase remains inert to reduction and oxidation, this results in a decrease of oxygen available for reaction and hence lowering of the oxygen storage capacity. The second type of deactivation, segregation of Fe from Ce_{1-x}Fe_xO_{2-x} leads to destruction of the solid solution and higher reduction temperatures for CeO₂, which is not beneficial for the redox process^{16, 54, 55}.

4.1.1 Perovskite formation (CeFeO₃)

To assess the influence of CeFeO₃ on the redox properties during cycling, pretreated 50wt%Fe₂O₃-CeO₂ was investigated using in situ XRD. The peak position analysis of CeFeO₃ (112) during H₂-TPR and CO₂-TPO (Supplementary info Figure S4) showed a steady shift towards lower two theta values, due to thermal lattice expansion. Hence, the perovskite phase didn't show reducibility in the given temperature range, and the formation of CeFeO₃ only led to loss of active metal available for reaction.

4.1.2 Segregation of Fe

For as prepared materials, Ce-K EXAFS modelling revealed around 21mol% of Ce substituted by Fe inside Ce_{1-x}Fe_xO_{2-x}. TEM images show the presence of atomically dispersed Fe throughout CeO₂, while the CeO₂ lattice parameter calculations from XRD indicate that an amount of Fe was incorporated inside the lattice of CeO₂ (Supplementary info Figure S1).

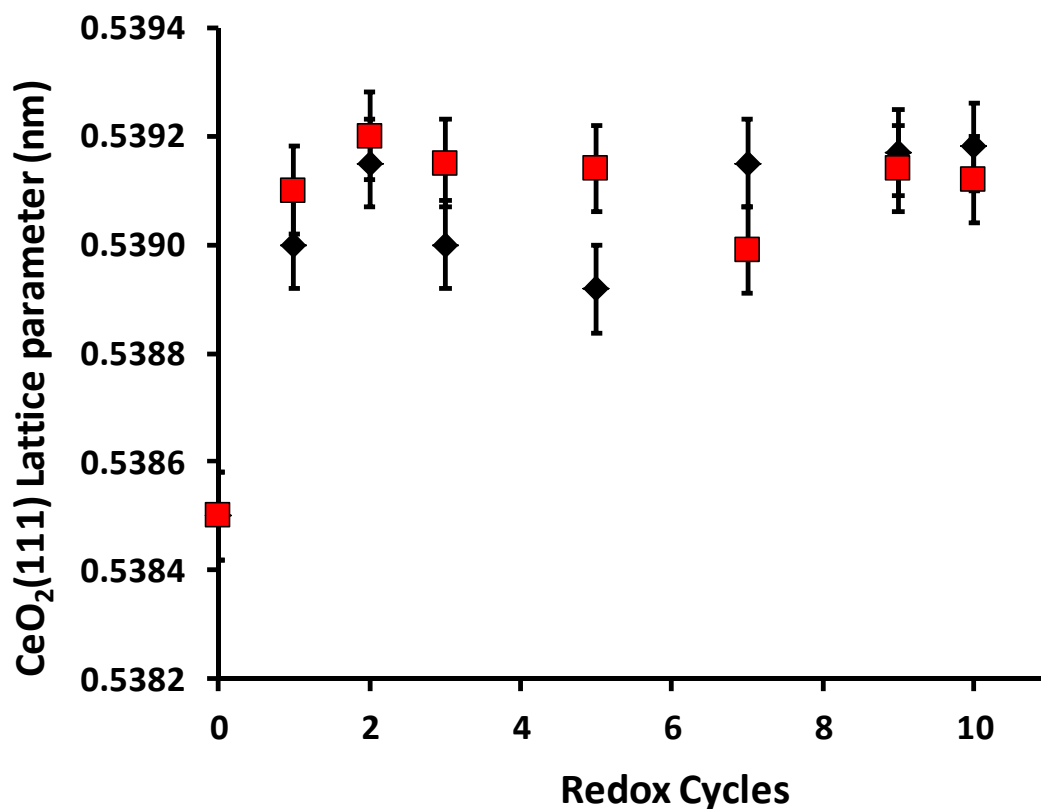


Figure 9: The CeO₂ lattice parameters of cycled 10wt% Fe₂O₃-CeO₂ and 80wt%Fe₂O₃-CeO₂ as a function of cycles Lattice parameters of (■) 80wt%Fe₂O₃-CeO₂ and (◆) 10wt%Fe₂O₃-CeO₂. The error bars represent standard error (68% confidence interval) calculated from 3 most intense peaks.

In previous work on 5wt%Fe₂O₃-CeO₂, agglomeration of segregated Fe was observed in TEM after 10 redox cycles, leading to nanoclusters at the CeO₂ grain boundaries²³. To further investigate the phenomenon of Fe segregation, lattice parameter calculations were performed after each redox cycle (Figure 9). It turned out that Fe was segregated from the CeO₂ lattice upon the very first redox cycle, while for subsequent cycles, the lattice parameter levelled off between 0.5389-0.5392nm. When comparing these values to those after 100 cycles (Table 1), it appears that the unit cell parameters do increase further, from 0.5389-0.5392nm at cycle 10 (Figure 9) to

1
2
3 0.5401nm upon cycle 100 (Table 1). This indicates that an amount of Fe is segregated easily in
4 the first redox cycle, but further withdrawal of Fe proceeds much slower.
5
6

7
8 The effect of Fe segregation upon the redox properties of the material can be twofold. On the one
9 hand, it destroys the solid solution $Ce_{1-x}Fe_xO_{2-x}$, which in turn will lead to more elevated redox
10 temperatures and enhanced sintering for CeO_2 . On the other hand, the segregated Fe can
11 contribute to the redox capacity of iron oxides, but is also likely to suffer from sintering.
12
13
14
15
16
17
18
19

20 21 **4.2 Sintering**

22
23 During sintering the overall oxygen available remains unchanged, but the increased diffusion
24 time of oxygen from the bulk to the surface leads to a loss of CO yield. To assess when the effect
25 of sintering sets in, the change in crystallite size of both CeO_2 and Fe_3O_4 was determined as a
26 function of cycles (Figure 10). Sintering of iron oxide is more rapid in 10wt% Fe_2O_3 - CeO_2 than
27 in 80wt% Fe_2O_3 - CeO_2 (Figure 10). For 10wt% Fe_2O_3 - CeO_2 , the increase in crystallite size of iron
28 oxide is especially steep after the first cycle: from 5nm Fe_2O_3 particles in as prepared material to
29 ~30nm Fe_3O_4 after 1 redox cycle. This huge size increase will relate not only to sintering of the
30 Fe_2O_3 nanoparticles originally present, but also to Fe segregated from CeO_2 , as an important
31 fraction of Fe is segregated from $Ce_{1-x}Fe_xO_{2-x}$ after the first cycle (Figure 9). For further redox
32 cycles, crystal growth continues but after cycle 10, the size is already close to the value after 100
33 cycles (Table 1). In parallel to Fe_3O_4 particle size growth, also CeO_2 sinters, possibly more
34 rapidly as the solid solution between Ce and Fe deteriorates.
35
36
37
38
39
40
41
42
43
44
45
46
47
48
49
50
51
52
53
54
55
56
57
58
59
60

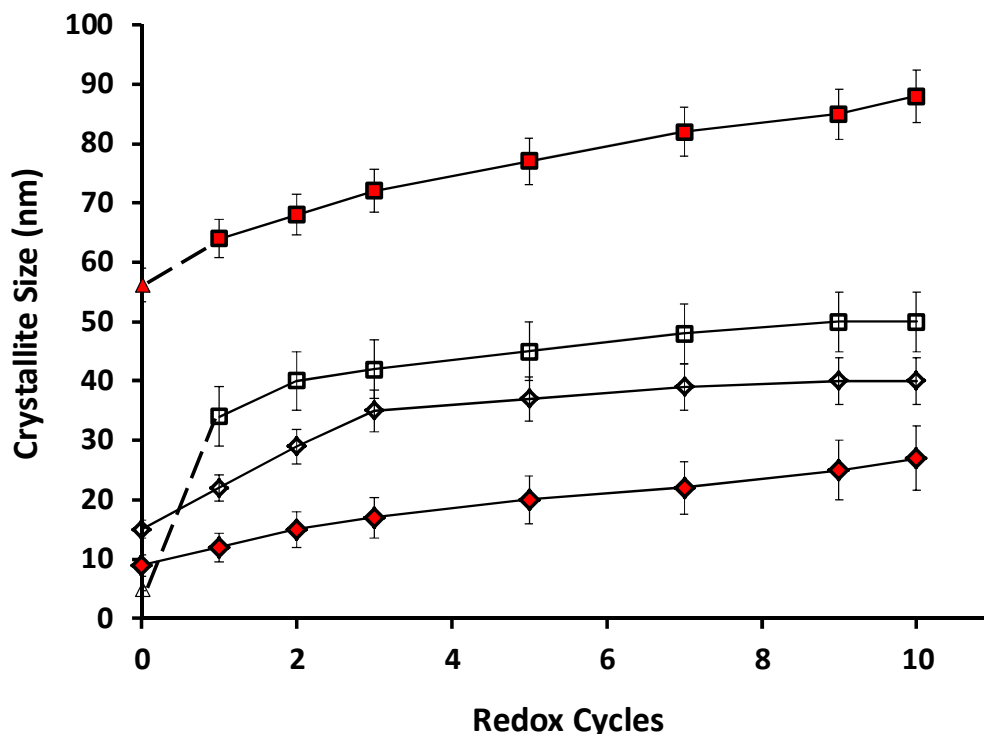


Figure 10: Crystallite sizes of CeO₂ and Fe₃O₄ during the first 10 redox cycles of 10wt%Fe₂O₃-CeO₂ and 80wt%Fe₂O₃-CeO₂. (Δ) Fe₂O₃ in as prepared material, (\square) Fe₃O₄ and (\diamond) CeO₂ crystallite sizes in 10wt%Fe₂O₃-CeO₂. (\blacktriangle) Fe₂O₃ in as prepared material, (\blacksquare) Fe₃O₄ and (\blacklozenge) CeO₂ crystallite sizes in 80wt%Fe₂O₃-CeO₂ (-----) guide for crystallite size evolution from Fe₂O₃ to Fe₃O₄, (—) guide to the eye for crystallite size increase between similar phase. Error bars represent standard deviation (68% confidence interval) calculated from 3 most intense peaks.

In 80wt%Fe₂O₃-CeO₂, large particles of Fe₂O₃ are present from the start with Ce_{1-x}Fe_xO_{2-x} as physical barrier in between them. Sintering of Fe₃O₄ in the first 10 cycles is less severe than in 10wt%Fe₂O₃-CeO₂. From the value after 100 cycles (Table 1) it follows that particle size will keep increasing throughout cycling operation. However, compared to pure iron oxide the loss in CO yield is significantly reduced²⁴. For the solid solution Ce_{1-x}Fe_xO_{2-x}, particle sizes increase

1
2
3 mostly in the first 10 cycles, i.e. when Fe is segregated from the lattice, but remain relatively
4 stable afterwards (Table 1).
5
6
7

8 9 **4.3 Deactivation of 10wt%Fe₂O₃-CeO₂ and 80wt% Fe₂O₃-CeO₂**

10 Different forms of deactivation have been identified in 10wt%Fe₂O₃-CeO₂ and 80wt% Fe₂O₃-
11 CeO₂: solid-solid transformation to perovskite (CeFeO₃), segregation of Fe, and sintering, each
12 playing a role in the loss of CO yield. The way in which each mechanism of deactivation affects
13 the materials largely depends on their bulk composition. In 10wt%Fe₂O₃-CeO₂, CeO₂ is the bulk
14 oxygen storage carrier, while in 80wt% Fe₂O₃-CeO₂ it is Fe₂O₃ and these will largely determine
15 the behaviour of the oxygen storage material in a chemical looping process.
16
17

18 In 10wt%Fe₂O₃-CeO₂, iron oxide promotes the active material by enhancing the redox properties
19 of CeO₂. The latter is achieved by the dissolution of Fe into the lattice of CeO₂, thereby creating
20 vacancies that facilitate the oxygen mobility and allow easy diffusion of oxygen from the bulk.
21 The resulting solid solution Ce_{1-x}Fe_xO_{2-x} is known for its enhanced redox properties. Upon
22 prolonged cycling of 10wt%Fe₂O₃-CeO₂, deactivation occurs due to sintering, perovskite
23 formation and segregation of Fe from Ce_{1-x}Fe_xO_{2-x}. In a redox atmosphere, Fe segregates out of
24 the lattice of CeO₂ and sinters rapidly along with CeO₂, in parallel to the perovskite phase
25 transformation. This results in loss of reducibility as observed in TPR and TPO of the cycled
26 material (Figure 7e and 8a). The deactivation in 10wt%Fe₂O₃-CeO₂ materials is summarized in
27 Figure 11a.
28
29

30 In 80wt%Fe₂O₃-CeO₂, Fe₃O₄ is the bulk oxygen carrier and CeO₂ acts as chemically active
31 promoter. In as prepared material, Ce_{1-x}Fe_xO_{2-x} solid solution particles decorate the larger iron
32 oxide crystallites (Figure 3). After cycling, all particle sizes have increased but the overall
33 structure of decoration remains unchanged. A distinct perovskite phase is not observed, but
34
35
36
37
38
39
40
41
42
43
44
45
46
47
48
49
50
51
52
53
54
55
56
57
58
59
60

cannot be excluded. Overall, the reducibility of this sample is largely preserved after cycling (Figure 6e and 8c). The role of the decorating CeO_2 crystallites is mainly preventing physical contact of iron oxide with only limited contribution to the oxygen storage capacity. The behavior of 80wt% Fe_2O_3 - CeO_2 can be represented as in Figure 11b.

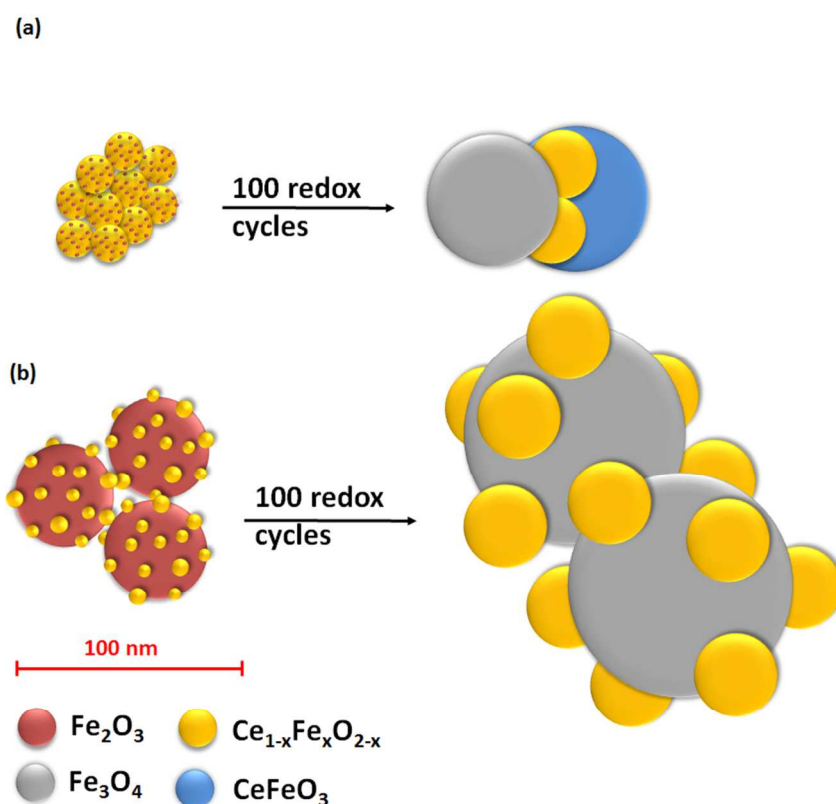


Figure 11: Deactivation in (a) 10wt% Fe_2O_3 - CeO_2 and (b) 80wt% Fe_2O_3 - CeO_2 after 100 redox cycles.

4.4 Material deactivation: what to do?

To counter the observed types of deactivation, several options are available. The formation of a perovskite phase in 10wt% Fe_2O_3 - CeO_2 or similar CeO_2 -rich materials can be avoided by applying a regeneration process. In contrast to CO_2 -TPO, O_2 -TPO is capable to decompose perovskite and restore the redox phases. The material is decomposed into CeO_2 and Fe_2O_3 .

1
2
3 around 400°C. Figure 12 confirms that for both materials, an O₂ treatment is beneficial to the CO
4 yield. An increase is observed in 10wt%Fe₂O₃-CeO₂ (Figure 12). In this material, a significant
5 perovskite phase is present after cycling, as evidenced by XRD (Figure 2b(ii)). Similar to pre-
6 treated 50wt%Fe₂O₃-CeO₂, the O₂ treatment likely decomposes the perovskite (CeFeO₃)
7 structure and leads to the regeneration of the oxygen carriers Fe₂O₃ and CeO₂, with
8 corresponding restoring of the CO yield. However, the regeneration does not bring back the
9 original CO yield and moreover, it is lost very rapidly when cycling is continued. Hence, loss of
10 oxygen storage capacity due to perovskite formation is an important deactivation pathway in this
11 sample.
12
13
14
15
16
17
18
19
20
21
22
23

24 In 80wt%Fe₂O₃-CeO₂ hardly any increase in the CO yield upon O₂ treatment was observed. This
25 could be related to the fact that the perovskite (CeFeO₃) being less present after cycling this
26 material (Figure 2b(i)). Unlike in 10wt%Fe₂O₃-CeO₂, perovskite formation is not the cause of
27 CO yield degeneration in 80wt%Fe₂O₃-CeO₂, which will mainly proceed through other forms of
28 deactivation.
29
30
31
32
33
34
35

36 The effect of deactivation due to sintering appears from the regeneration study of the samples
37 (Figures 12 and Figure 1). Despite the restoration of Fe₂O₃ and CeO₂ phases by means of O₂
38 treatment, the materials could not regain the CO yield of the as prepared materials because of the
39 increased crystallite size. For Fe₂O₃-rich materials, sintering is the dominant process to be
40 countered.
41
42
43
44
45
46
47
48
49
50
51
52
53
54
55
56
57
58
59
60

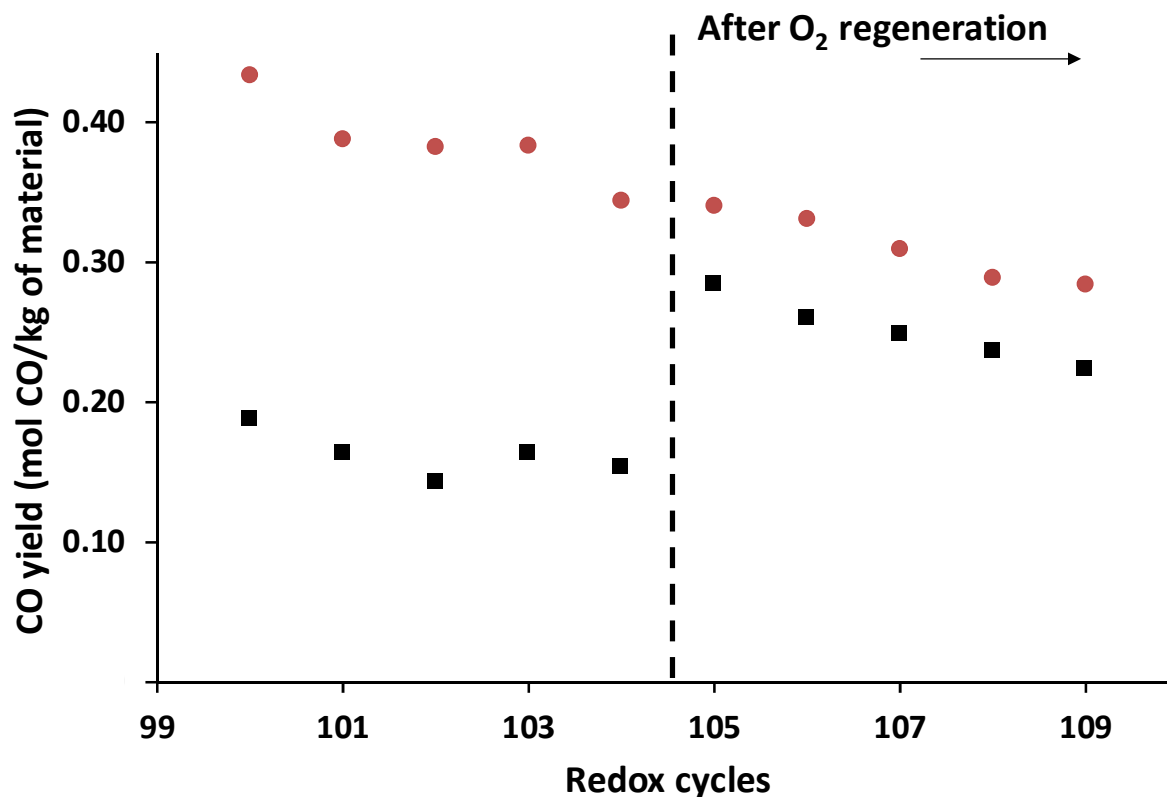


Figure 12: Regeneration study of 10wt%Fe₂O₃-CeO₂ and 80wt%Fe₂O₃-CeO₂ by means of O₂ treatment. (■) 10wt%Fe₂O₃-CeO₂ and (●) 80wt%Fe₂O₃-CeO₂.

Sintering is physical process which leads to the loss of material surface due to crystallite growth of either the support material or the active phase. Sintering is strongly temperature dependent. The core mechanism is surface diffusion, or, at sufficiently high temperature, mobility of larger aggregates. This leads to a correlation with the melting point. The solid-state diffusion becomes faster when the temperature is closer to the melting point. The so-called Hüttig and Tamman temperatures are indicative for the temperature at which sintering may occur. When the Hüttig temperature is reached, atoms at defects will become mobile. At the Tamman temperature, atoms from the bulk will show mobility, while at the melting temperature, overall mobility will be

1
2
3 really high. The following empirical relations for the Hüttig and Tamman temperatures are
4 recommended for use:
5

$$6 \quad T_{\text{Hüttig}} = 0.3T_{\text{melting}}$$

$$7 \quad T_{\text{Tamman}} = 0.5T_{\text{melting}}$$

8
9
10 In the reducing and oxidizing atmosphere of a chemical looping process, the thermal stability of
11 the material changes depending on the material state. For example, the melting temperatures for
12 Fe_2O_3 , Fe_3O_4 , FeO and Fe are 1565°C , 1597°C , 1377°C and 1538°C respectively. The formation
13 of FeO during the reduction/oxidation process will naturally decrease the material melting
14 temperature, which can lead to fast material sintering. Sintering is best avoided by minimizing
15 and controlling the temperature of reaction, although recent developments have focused on
16 encapsulating metal crystallites to eliminate mobility, while still allowing access for reactants
17 and products.
18
19

20 The decoration of Fe_2O_3 with small CeO_2 crystallites provides a valid strategy for reduced
21 sintering but could be improved. Various promoter materials can be used for this approach, but
22 most of them give rise to solid-solid transformation leading to lower CO production. The
23 properties of CeO_2 can be further enhanced by adding a second element, e.g. ZrO_2 , CeZrO_2 .
24 Those materials presents high resistance to sintering and in addition, will not form a perovskite
25 phase with iron oxide.
26
27
28
29
30
31
32
33
34
35
36
37
38
39
40
41
42
43
44
45
46
47
48

49 **5.0 Conclusions**

50
51 10wt% Fe_2O_3 - CeO_2 and 80wt% Fe_2O_3 - CeO_2 oxygen storage materials were subjected to
52 prolonged redox cycling to study their deactivation. Three types of deactivation were identified:
53 sintering, Fe segregation from solid solution and perovskite formation, leading to a loss of CO
54
55
56
57
58
59
60

1
2
3 yield. The segregation of Fe from the $Ce_{1-x}Fe_xO_{2-x}$ occurs very fast, from the first redox cycle on.
4
5 It leads to lower reducibility of CeO_2 , but at the same time provides more iron oxide storage
6
7 capacity after decomposition of perovskite ($CeFeO_3$) resulting in more reducible Fe. Perovskite
8
9 ($CeFeO_3$) forms in the first tens of cycles and leads to a loss of oxygen storage capacity as it is
10
11 non-reducible. Sintering then again is a slower process which continues throughout cyclic
12
13 operation. It causes crystallites to grow in size, thereby increasing the diffusion time of bulk
14
15 oxygen to the surface. Hence, a lower degree of reduction is reached and upon reoxidation a
16
17 lower CO yield is obtained.
18
19
20

21
22 The relative importance of these deactivation types depends on the composition of the oxygen
23
24 storage material. In 80wt% Fe_2O_3 - CeO_2 deactivation is predominantly caused by sintering of iron
25
26 oxides. Fe segregation is of minor importance given the composition of this material. Similarly,
27
28 perovskite formation may possibly occur, but will hardly affect the cycling productivity. In
29
30 10wt% Fe_2O_3 - CeO_2 all three types of deactivation are at play, this is why deactivation for this
31
32 composition is more rapid and severe during the first 10 cycles.
33
34
35

36
37 A regeneration study shows that after treatment with O_2 , the CO yield for both materials
38
39 increases slightly. The increase in the CO yield is more prominent in 10wt% Fe_2O_3 - CeO_2 , where
40
41 the O_2 treatment leads to decomposition and phase segregation of $CeFeO_3$. However, the overall
42
43 CO yield remains lower than at the start of cycling, showing the importance of sintering in this
44
45 material.
46
47

48
49 In terms of CO yield, 80wt% Fe_2O_3 - CeO_2 stands out as the best material for prolonged cycling. In
50
51 this material, the main deactivation type sintering is reduced by the strategy of decorating Fe_2O_3
52
53 with CeO_2 nanoparticles. Based on this deactivation study, replacing CeO_2 with a compound that
54
55
56
57
58
59
60

1
2
3 does not undergo solid-solid transformations, could prove worthwhile in view of further
4
5
6 countering deactivation.
7

8 9 **Acknowledgements**

10
11 This work was supported by the Long Term Structural Methusalem Funding by the Flemish
12 Government, the Fund for Scientific Research Flanders (FWO; project G004613N) and The
13 Interuniversity Attraction Poles Programme, IAP7/5 Belgian State – Belgian Science Policy
14 (BELSPO). The authors acknowledge the Fund for Scientific Research Flanders (FWO-
15 Vlaanderen) in supplying financing of beam time at the DUBBLE and SNBL beam line of the
16 ESRF and travel costs. The authors also thank the assistance of the DUBBLE and SNBL staff
17 and equally acknowledge the technical support from Geert Rampelberg with the in situ XRD
18 equipment (Department of Solid State Sciences, Ghent University).
19
20
21
22
23
24
25
26
27

28 **Supporting Information**

29
30 Lattice parameter evolution (Figure S1), in situ XRD during CO₂-TPO of 10wt%Fe₂O₃-CeO₂
31 (Figure S2a&b), in situ XRD during CO₂-TPO of 80wt%Fe₂O₃-CeO₂ (Figure S3a&b), CeFeO₃
32 peak position (Figure S4).
33
34
35
36
37
38
39
40

41 **References**

- 42
43 1. Chueh, W. C.; Falter, C.; Abbott, M.; Scipio, D.; Furler, P.; Haile, S. M.; Steinfeld, A., High-Flux
44 Solar-Driven Thermochemical Dissociation of CO₂ and H₂O Using Nonstoichiometric Ceria.
45 Science 2010, 330, 1797-1801.
- 46
47 2. Du, N.; Park, H. B.; Robertson, G. P.; Dal-Cin, M. M.; Visser, T.; Scoles, L.; Guiver, M. D.,
48 Polymer nanosieve membranes for CO₂-capture applications. Nat. Mater. 2011, 10, 372-375.
- 49
50 3. Yang, H.; Xu, Z.; Fan, M.; Gupta, R.; Slimane, R. B.; Bland, A. E.; Wright, I., Progress in carbon
51 dioxide separation and capture: A review. J. Environ. Sci. 2008, 20, 14-27.
- 52
53 4. Sheps, K. M.; Max, M. D.; Osegovic, J. P.; Tatro, S. R.; Brazel, L. A., A case for deep-ocean CO₂
54 sequestration. Energy Procedia 2009, 1, 4961-4968.
- 55
56 5. Doucet, F. J., Effective CO₂-specific sequestration capacity of steel slags and variability in their
57 leaching behaviour in view of industrial mineral carbonation. Miner. Eng. 2010, 23, 262-269.
58
59
60

6. Shao, H.; Ray, J. R.; Jun, Y.-S., Dissolution and Precipitation of Clay Minerals under Geologic CO₂ Sequestration Conditions: CO₂-Brine-Phlogopite Interactions. *Environ. Sci. Technol.* 2010, 44, 5999-6005.
7. Zhang, W. E. I., Density-driven enhanced dissolution of injected CO₂ during long-term CO₂ geological storage. *J. Earth Syst. Sci.* 2013, 122, 1387-1397.
8. Khoo, H. H.; Tan, R. B. H., Environmental impact evaluation of conventional fossil fuel production (oil and natural gas) and enhanced resource recovery with potential CO₂ sequestration. *Energy Fuels* 2006, 20, 1914-1924.
9. Galvita, V. V.; Poelman, H.; Marin, G. B., Combined chemical looping for energy storage and conversion. *J. Power Sources* 2015, 286, 362-370.
10. Fan, L. S.; Zeng, L.; Wang, W. L.; Luo, S. W., Chemical looping processes for CO₂ capture and carbonaceous fuel conversion - prospect and opportunity. *Energy Environ. Sci.* 2012, 5, 7254-7280.
11. Bhavsar, S.; Najera, M.; Vesper, G., Chemical Looping Dry Reforming as Novel, Intensified Process for CO₂ Activation. *Chem. Eng. Technol.* 2012, 35, 1281-1290.
12. Fan, L. S.; Zeng, L.; Luo, S. W., Chemical Looping Rises to the Challenge. *Chem. Eng. Prog.* 2015, 111, 30-38.
13. Dai, X. P.; Li, J.; Fan, J. T.; Wei, W. S.; Xu, J., Synthesis Gas Generation by Chemical-Looping Reforming in a Circulating Fluidized Bed Reactor Using Perovskite LaFeO₃-Based Oxygen Carriers. *Ind. Eng. Chem. Res.* 2012, 51, 11072-11082.
14. Cabello, A.; Dueso, C.; Garcia-Labiano, F.; Gayan, P.; Abad, A.; de Diego, L. F.; Adanez, J., Performance of a highly reactive impregnated Fe₂O₃/Al₂O₃ oxygen carrier with CH₄ and H₂S in a 500 W-th CLC unit. *Fuel* 2014, 121, 117-125.
15. Galvita, V. V.; Poelman, H.; Detavernier, C.; Marin, G. B., Catalyst-assisted chemical looping for CO₂ conversion to CO. *Appl. Catal., B* 2015, 164, 184-191.
16. Galvita, V. V.; Poelman, H.; Bliznuk, V.; Detavernier, C.; Marin, G. B., CeO₂-Modified Fe₂O₃ for CO₂ Utilization via Chemical Looping. *Ind. Eng. Chem. Res.* 2013, 52, 8416-8426.
17. Lyngfelt, A., Oxygen Carriers for Chemical Looping Combustion-4000 h of Operational Experience. *Oil Gas Sci. Technol.* 2011, 66, 161-172.
18. Bayham, S.; McGiveron, O.; Tong, A.; Chung, E.; Kathe, M.; Wang, D. W.; Zeng, L.; Fan, L. S., Parametric and dynamic studies of an iron-based 25-kW(th) coal direct chemical looping unit using sub-bituminous coal. *Appl. Energy* 2015, 145, 354-363.
19. A. Tong, S. Bayham, M.V. Kathe, L. Zeng, S. Luo, L.-S. Fan, Iron-based syngas chemical looping process and coal-direct chemical looping process development at Ohio State University, *Appl. Energy*, 2014, 113, 1836-1845.
20. Galvita, V.; Hempel, T.; Lorenz, H.; Rihko-Struckmann, L. K.; Sundmacher, K., Deactivation of modified iron oxide materials in the cyclic water gas shift process for CO-free hydrogen production. *Ind. Eng. Chem. Res.* 2008, 47, 303-310.
21. Datta, P.; Rihko-Struckmann, L. K.; Sundmacher, K., Influence of molybdenum on the stability of iron oxide materials for hydrogen production with cyclic water gas shift process. *Mater. Chem. Phys.* 2011, 129, 1089-1095.
22. Galvita, V. V.; Filez, M.; Poelman, H.; Bliznuk, V.; Marin, G. B., The Role of Different Types of CuO in CuO-CeO₂/Al₂O₃ for Total Oxidation. *Catal. Lett.* 2014, 144, 32-43.

23. Meledina, M.; Turner, S.; Galvita, V. V.; Poelman, H.; Marin, G. B.; Van Tendeloo, G., Local environment of Fe dopants in nanoscale Fe : CeO_{2-x} oxygen storage material. *Nanoscale* 2015, 7, 3196-3204.
24. Galvita, V.; Sundmacher, K., Redox behavior and reduction mechanism of Fe₂O₃-CeZrO₂ as oxygen storage material. *J. Mater. Sci.* 2007, 42, 9300-9307.
25. Mattisson, T.; Lyngfelt, A.; Cho, P., The use of iron oxide as an oxygen carrier in chemical-looping combustion of methane with inherent separation of CO₂. *Fuel* 2001, 80, 1953-1962.
26. Kidambi, P. R.; Cleeton, J. P. E.; Scott, S. A.; Dennis, J. S.; Bohn, C. D., Interaction of Iron Oxide with Alumina in a Composite Oxygen Carrier during the Production of Hydrogen by Chemical Looping. *Energy Fuels* 2012, 26, 603-617.
27. Kierzkowska, A. M.; Bohn, C. D.; Scott, S. A.; Cleeton, J. P.; Dennis, J. S.; Muller, C. R., Development of Iron Oxide Carriers for Chemical Looping Combustion Using Sol-Gel. *Ind. Eng. Chem. Res.* 2010, 49, 5383-5391.
28. Galvita, V. V.; Poelman, H.; Marin, G. B., Hydrogen Production from Methane and Carbon Dioxide by Catalyst-Assisted Chemical Looping. *Top. Catal.* 2011, 54, 907-913.
29. Zafar, Q.; Mattisson, T.; Gevert, B., Integrated hydrogen and power production with CO₂ capture using chemical-looping reforming-redox reactivity of particles of CuO, Mn₂O₃, NiO, and Fe₂O₃ using SiO₂ as a support. *Ind. Eng. Chem. Res.* 2005, 44, 3485-3496.
30. Corbella, B. M.; Palacios, J. M., Titania-supported iron oxide as oxygen carrier for chemical-looping combustion of methane. *Fuel* 2007, 86, 113-122.
31. Leion, H.; Mattisson, T.; Lyngfelt, A., The use of petroleum coke as fuel in chemical-looping combustion. *Fuel* 2007, 86, 1947-1958.
32. Shulman, A.; Linderholm, C.; Mattisson, T.; Lyngfelt, A., High Reactivity and Mechanical Durability of NiO/NiAl₂O₄ and NiO/NiAl₂O₄/MgAl₂O₄ Oxygen Carrier Particles Used for more than 1000 h in a 10 kW CLC Reactor. *Ind. Eng. Chem. Res.* 2009, 48, 7400-7405.
33. Johansson, M.; Mattisson, T.; Lyngfelt, A., Investigation of Fe₂O₃ with MgAl₂O₄ for chemical-looping combustion. *Ind. Eng. Chem. Res.* 2004, 43, 6978-6987.
34. Dharanipragada, N. V. R. A.; Buelens, L. C.; Poelman, H.; De Grave, E.; Galvita, V. V.; Marin, G. B., Mg-Fe-Al-O for advanced CO₂ to CO conversion: carbon monoxide yield vs. oxygen storage capacity. *J. Mater. Chem. A* 2015, 3, 16251-16262.
35. Rihko-Struckmann, L. K.; Datta, P.; Wenzel, M.; Sundmacher, K.; Dharanipragada, N. V. R. A.; Poelman, H.; Galvita, V. V.; Marin, G. B., Hydrogen and Carbon Monoxide Production by Chemical Looping over Iron-Aluminium Oxides. *Energy Technol.* 2015, 3, 1-11.
36. Bobin, A. S.; Sadykov, V. A.; Rogov, V. A.; Mezentseva, N. V.; Alikina, G. M.; Sadovskaya, E. M.; Glazneva, T. S.; Sazonova, N. N.; Smirnova, M. Y.; Veniaminov, S. A.; Mirodatos, C.; Galvita, V.; Marin, G. B., Mechanism of CH₄ Dry Reforming on Nanocrystalline Doped Ceria-Zirconia with Supported Pt, Ru, Ni, and Ni-Ru. *Top. Catal.* 2013, 56, 958-968.
37. Galinsky, N. L.; Shafiefarhood, A.; Chen, Y.; Neal, L.; Li, F., Effect of support on redox stability of iron oxide for chemical looping conversion of methane. *Appl. Catal., B* 2015, 164, 371-379.
38. Tang, M.; Xu, L.; Fan, M., Progress in oxygen carrier development of methane-based chemical-looping reforming: A review. *Appl. Energy* 2015, 151, 143-156.
39. Zhu, X.; Li, K.; Wei, Y.; Wang, H.; Sun, L., Chemical-Looping Steam Methane Reforming over a CeO₂-Fe₂O₃ Oxygen Carrier: Evolution of Its Structure and Reducibility. *Energy Fuels* 2014, 28, 754-760.

- 1
2
3
4
5
6
7
8
9
10
11
12
13
14
15
16
17
18
19
20
21
22
23
24
25
26
27
28
29
30
31
32
33
34
35
36
37
38
39
40
41
42
43
44
45
46
47
48
49
50
51
52
53
54
55
56
57
58
59
60
40. Ravel, B.; Newville, M., ATHENA and ARTEMIS: Interactive graphical data analysis using IFEFFIT. *Phys. Scr.* 2005, T115, 1007-1010.
 41. Koningsberger, D. C.; Mojet, B. L.; van Dorssen, G. E.; Ramaker, D. E., XAFS spectroscopy; fundamental principles and data analysis. *Top. Catal.* 2000, 10, 143-155.
 42. J.J. Rehr, J.M. Deleon, S.I. Zabinsky, R.C. Albers, Theoretical X-Ray Absorption Fine-Structure Standards, *J. Am. Chem. Soc.* 1991, 113, 5135-5140.
 43. Hamilton, W. C., Significance Tests on Crystallographic R Factor. *Acta Crystallogr. A* 1965, 18, 502-&.
 44. Bacchi, A.; Lamzin, V. S.; Wilson, K. S., A self-validation technique for protein structure refinement: The extended Hamilton test. *Acta Crystallogr D* 1996, 52, 641-646.
 45. Zielinski, J.; Zglinicka, I.; Znak, L.; Kaszukur, Z., Reduction of Fe₂O₃ with hydrogen. *Appl. Catal., A* 2010, 381, 191-196.
 46. Rampelberg, G.; De Schutter, B.; Devulder, W.; Martens, K.; Radu, I.; Detavernier, C., In situ X-ray diffraction study of the controlled oxidation and reduction in the V-O system for the synthesis of VO₂ and V₂O₃ thin films . *J. Mater. Chem. C* 2015, 3, 11357-11365.
 47. Theofanidis, S. A.; Galvita, V. V.; Poelman, H.; Marin, G. B., Enhanced Carbon-Resistant Dry Reforming Fe-Ni Catalyst: Role of Fe. *ACS Catal.* 2015, 5, 3028-3039.
 48. Galvita, V. V.; Poelman, H.; Rampelberg, G.; De Schutter, B.; Detavernier, C.; Marin, G. B., Structural and Kinetic Study of the Reduction of CuO-CeO₂/Al₂O₃ by Time-Resolved X-ray Diffraction. *Catal. Lett.* 2012, 142, 959-968.
 49. Redekop, E. A.; Galvita, V. V.; Poelman, H.; Bliznuk, V.; Detavernier, C.; Marin, G. B., Delivering a Modifying Element to Metal Nanoparticles via Support: Pt-Ga Alloying during the Reduction of Pt/Mg(Al,Ga)O_x Catalysts and Its Effects on Propane Dehydrogenation. *ACS Catal.* 2014, 4, 1812-1824.
 50. Galinsky, N. L.; Shafiefarhood, A.; Chen, Y.; Neal, L.; Li, F., Effect of support on redox stability of iron oxide for chemical looping conversion of methane. *Appl. Catal., B* 2015, 164, 371-379.
 51. Li, K. Z.; Wang, H.; Wei, Y. G.; Zhu, X., Structural Features of Ce-Fe Mixed Oxide and Its Applications in Catalysis. *Prog. Chem.* 2013, 25, 1691-1702.
 52. Zhu, X.; Li, K. Z.; Wei, Y. G.; Wang, H.; Sun, L. Y., Chemical-Looping Steam Methane Reforming over a CeO₂-Fe₂O₃ Oxygen Carrier: Evolution of Its Structure and Reducibility. *Energy Fuels* 2014, 28, 754-760.
 53. Gu, Z. H.; Li, K. Z.; Qing, S.; Zhu, X.; Wei, Y. G.; Li, Y. T.; Wang, H., Enhanced reducibility and redox stability of Fe₂O₃ in the presence of CeO₂ nanoparticles. *RSC Adv.* 2014, 4, 47191-47199.
 54. Moog, I.; Prestipino, C.; Figueroa, S.; Majimel, J.; Demourgues, A., Dual Ce⁴⁺/Fe³⁺ Redox Phenomena into Nanocrystalline Ce_{1-x}Fe_xO_{2-x/2} Solid Solution. *J. Phys. Chem. C* 2014, 118, 22746-22753.
 55. Moog, I.; Feral-Martin, C.; Duttine, M.; Wattiaux, A.; Prestipino, C.; Figueroa, S.; Majimel, J.; Demourgues, A., Local organization of Fe³⁺ into nano-CeO₂ with controlled morphologies and its impact on reducibility properties. *J. Mater. Chem. A* 2014, 2, 20402-20414.
 56. Theofanidis, S. A.; Batchu, R.; Galvita, V. V.; Poelman, H.; Marin, G. B., Carbon gasification from Fe-Ni catalysts after methane dry reforming. *Appl. Catal., B* 2016, 185, 42-55.

